

## RESEARCH ARTICLE

10.1002/2014GC005566

## Key Points:

- MORB fission Xe isotopes indicate MORB source is more degassed than plume source
- Recycled atmospheric Xe shows sampled reservoirs not pristine primordial mantle
- Xe recycling has not overprinted ancient differences evident in MORBs and plumes

## Supporting Information:

- Supporting Information

## Correspondence to:

R. Parai,  
rparai@carnegiescience.edu

## Citation:

Parai, R., and S. Mukhopadhyay (2015), The evolution of MORB and plume mantle volatile budgets: Constraints from fission Xe isotopes in Southwest Indian Ridge basalts, *Geochem. Geophys. Geosyst.*, 16, doi:10.1002/2014GC005566.

Received 5 SEP 2014

Accepted 20 JAN 2015

Accepted article online 28 JAN 2015

## The evolution of MORB and plume mantle volatile budgets: Constraints from fission Xe isotopes in Southwest Indian Ridge basalts

Rita Parai<sup>1,2</sup> and Sujoy Mukhopadhyay<sup>3</sup>

<sup>1</sup>Department of Earth and Planetary Sciences, Harvard University, Cambridge, Massachusetts, USA, <sup>2</sup>Department of Terrestrial Magnetism, Carnegie Institution for Science, Washington, District of Columbia, USA, <sup>3</sup>Department of Earth and Planetary Sciences, University of California, Davis, California, USA

**Abstract** We present high-precision measurements of the fission isotopes of xenon (Xe) in basalts from the Southwest Indian Ridge (SWIR) between 16°E and 25°E. Corrections for syn- to post-eruptive atmospheric contamination yield the Xe isotopic compositions of SWIR mantle sources. We solve for the proportions of mantle Xe derived from the primordial mantle Xe budget, recycling of atmospheric Xe, decay of short-lived <sup>129</sup>I, fission of extinct <sup>244</sup>Pu, and fission of extant <sup>238</sup>U. Xe isotope systematics evident in SWIR basalts and other mantle-derived samples provide new insights into the integrated history of mantle source degassing and regassing. We find that recycled atmospheric Xe dominates the Xe inventories of the SWIR Western and Eastern Orthogonal Supersegment mantle sources (~80–90% of <sup>132</sup>Xe is recycled in origin), consistent with results from studies of plume-influenced basalts from Iceland and the Rochambeau Rift. While significant regassing of the mantle is evident, we also find differences in the extent of degassing of the MORB and plume sources. MORB sources are consistently characterized by a lower fraction of fission Xe derived from Pu-fission, indicating a greater extent of degassing relative to the plume source. The prevalence of recycled atmospheric Xe in mantle sources indicates incorporation of depleted recycled material even into mantle sources with primitive He and Ne isotopic compositions. Consequently, depleted lithophile isotopic compositions in mantle sources with primitive He and Ne cannot be interpreted as evidence for a nonchondritic bulk silicate Earth.

### 1. Introduction

Noble gases are powerful tracers of deep Earth degassing and regassing. A diverse set of short-lived (<sup>129</sup>I, <sup>244</sup>Pu) and long-lived (<sup>235</sup>U, <sup>238</sup>U, <sup>232</sup>Th, <sup>40</sup>K) radioactive nuclides decay to produce specific noble gas isotopes, such that helium, neon, argon, and xenon isotopic compositions are variably sensitive to processes occurring on a range of time scales. In particular, the diverse array of radiogenic, fissionogenic, and primordial isotopes of Xe has the potential to provide new insights into the evolution of mantle volatile budgets. The light, stable, nonradiogenic isotopes <sup>124</sup>Xe, <sup>126</sup>Xe, <sup>128</sup>Xe, and <sup>130</sup>Xe are primordial; terrestrial inventories for these isotopes were established during accretion. Radiogenic <sup>129</sup>Xe was produced by  $\beta$ -decay of the extinct nuclide <sup>129</sup>I ( $t_{1/2} = 15.7$  Ma) in the first ~90 Myr of Earth history. Fissionogenic <sup>131</sup>Xe, <sup>132</sup>Xe, <sup>134</sup>Xe, and <sup>136</sup>Xe are produced in distinct, characteristic proportions by fission of extinct short-lived <sup>244</sup>Pu ( $t_{1/2} = 80.0$  Myr) and extant long-lived <sup>238</sup>U ( $t_{1/2} = 4.468$  Gyr). A full set of Xe isotopic compositions measured in mantle-derived samples can thus be used to investigate the evolution of mantle volatile budgets on a variety of time scales.

Noble gas isotope systematics in mid-ocean ridge basalts (MORBs) differ from those measured in plume-derived ocean island basalts (OIBs) [e.g., Graham, 2002; Hilton et al., 1999, 2000; Kurz et al., 1982a, 1982b; Moreira, 2013; Moreira et al., 1998; Mukhopadhyay, 2012; Parai et al., 2009, 2012; Pető et al., 2013; Trierloff et al., 2000; Tucker et al., 2012]. For example, MORB helium isotopic compositions typically fall within a range of <sup>4</sup>He/<sup>3</sup>He between ~80,000 and 100,000 (<sup>3</sup>He/<sup>4</sup>He ratios of ~7–9 R<sub>A</sub>, where R<sub>A</sub> signifies the atmospheric ratio [Graham et al., 1992; Kurz et al., 1982b; Moreira et al., 1998]). In contrast, plume helium isotopic signatures vary widely (<sup>4</sup>He/<sup>3</sup>He ratios ranging from ~15,000 to 200,000) [Farley et al., 1992; Graham, 2002; Hilton et al., 1999; Kurz and Geist, 1999; Kurz et al., 1983; Moreira et al., 1999; Stuart et al., 2003]. Low ratios of radiogenic <sup>4</sup>He to primordial <sup>3</sup>He (<sup>4</sup>He/<sup>3</sup>He < 50,000) in plume-derived samples from Iceland, Galapagos, and

Samoa are traditionally attributed to sampling of a plume source that has experienced less degassing and has thus retained a larger proportion of its primordial  $^3\text{He}$  budget relative to the MORB source [Farley *et al.*, 1992; Hilton *et al.*, 1999; Kurz and Geist, 1999; Kurz *et al.*, 1983; Moreira *et al.*, 1999; Stuart *et al.*, 2003]. Heavy noble gas isotope systematics in MORB and plume samples support the model of a plume source that has experienced less degassing relative to the MORB source: plume samples are characterized by relatively low ratios of nucleogenic  $^{21}\text{Ne}$ , radiogenic  $^{40}\text{Ar}$ , and radiogenic  $^{129}\text{Xe}$  to primordial  $^{20}\text{Ne}$ ,  $^{36}\text{Ar}$ , and  $^{130}\text{Xe}$ , respectively [Harrison *et al.*, 1999; Moreira *et al.*, 1998; Mukhopadhyay, 2012; Parai *et al.*, 2012; Pető *et al.*, 2013; Trieroff *et al.*, 2000; Tucker *et al.*, 2012].

Alternative models have been suggested to explain MORB and plume noble gas isotope systematics. Low plume  $^4\text{He}/^3\text{He}$  ratios have been attributed to the generation of low  $(\text{U} + \text{Th})/^3\text{He}$  in residues of partial melting [Parman *et al.*, 2005], or to early preservation of primordial  $(\text{U} + \text{Th})/^3\text{He}$  in Fe-rich partial melt products within the deep mantle [Lee *et al.*, 2010]. Holland and Ballentine [2006] suggest that low  $^{40}\text{Ar}/^{36}\text{Ar}$  and  $^{129}\text{Xe}/^{130}\text{Xe}$  in plume-related samples reflect preferential incorporation of recycled seawater-derived noble gases into the plume source relative to the MORB source. However, Mukhopadhyay [2012] and Pető *et al.* [2013] demonstrate that plume and MORB mantle sources cannot be related simply by differential regassing of atmospheric volatiles. Rather, based on the extinct  $^{129}\text{I}$ - $^{129}\text{Xe}$  system, the authors argue the plume source samples an ancient reservoir that separated from the MORB source within 100 Myr of the start of the Solar System [Mukhopadhyay, 2012; Parai *et al.*, 2012; Pető *et al.*, 2013; Tucker *et al.*, 2012]. In spite of observed plume He-Xe isotope systematics, Huang *et al.* [2014] hypothesized that plume He signatures reflect preferential sampling of primitive  $^4\text{He}/^3\text{He}$  frozen into sulfide-rich mafic cumulates generated at  $\sim 3$  Ga or later in association with continent formation. However, plume He-Xe signatures indicate that plumes sample noble gases from a source that separated from the MORB mantle prior to 4.45 Ga, and plume  $^4\text{He}/^3\text{He}$  signatures are associated with  $^3\text{He}/^{22}\text{Ne}$  ratios distinct from MORB that likely reflect differential degassing during the giant impact and magma ocean stage of early Earth history [Tucker and Mukhopadhyay, 2014]. The storage of primitive helium signatures in sulfides formed exclusively at 3 Ga or later proposed by Huang *et al.* is therefore not supported by the noble gas data.

Several authors have noted that low  $^4\text{He}/^3\text{He}$  ratios in mantle-derived basalts are associated with Nd isotopic signatures that are depleted relative to a chondritic bulk silicate Earth value [Class and Goldstein, 2005; Jackson and Carlson, 2011; Jackson *et al.*, 2010; Jackson and Jellinek, 2013]. Gonnermann and Mukhopadhyay [2009] demonstrated that mantle He-Nd systematics can be explained by differential incorporation of helium-poor recycled slabs with high Sm/Nd into both the MORB and plume sources over Earth history. In this case, degassed slabs with depleted trace element signatures are incorporated into a relatively gas-rich plume source over time, such that low  $^4\text{He}/^3\text{He}$  ratios are preserved in material that is not pristine primordial mantle. Alternately, high  $^{143}\text{Nd}/^{144}\text{Nd}$  ratios observed in samples with the lowest measured  $^4\text{He}/^3\text{He}$  ratios [Stuart *et al.*, 2003] have been interpreted as evidence that the primordial bulk silicate Earth may be nonchondritic [Jackson *et al.*, 2010].

Xe isotope systematics in mantle-derived samples have the potential to better constrain the nature of MORB and plume sources. The present-day mantle source Xe budget reflects a combination of primordial mantle Xe, recycled atmospheric Xe, decay of short-lived  $^{129}\text{I}$ , fission of short-lived  $^{244}\text{Pu}$ , and fission of extant  $^{238}\text{U}$ . High-precision Xe isotopic data may be assessed to determine the proportions of mantle source Xe derived from each of the components listed above. The relative proportion of Pu-fission Xe relative to U-fission Xe retained in a mantle source directly constrains the degree of degassing experienced by that source [Boulos and Manuel, 1971; Kunz *et al.*, 1998; Pepin and Porcelli, 2006; Phinney *et al.*, 1978]. Meanwhile, the proportion of mantle Xe derived from incorporation of recycled volatiles furnishes a test of the origin of depleted Nd isotopic compositions: if recycled slabs carry atmospheric volatiles, mixing of slabs into the MORB and plume source reservoirs has the potential to recycle significant amounts of atmospheric heavy noble gases to the deep Earth.

In this study, we present high-precision Xe isotopic data for a set of MORB glass samples dredged from the Southwest Indian Ridge (SWIR) Orthogonal Supersegment between  $16^\circ\text{E}$  and  $25^\circ\text{E}$  (Figure 1) [for major, trace element and helium data see Georgen *et al.*, 2003; Kurz *et al.*, 1998; Mahoney *et al.*, 1992; Standish, 2006; Standish *et al.*, 2008]. We are able to further characterize the extent of variability in MORB heavy noble gas signatures [Kunz *et al.*, 1998; Parai *et al.*, 2012; Tucker *et al.*, 2012]. Parai *et al.* [2012] found large magnitude variations in mantle source  $^{40}\text{Ar}/^{36}\text{Ar}$  and  $^{129}\text{Xe}/^{130}\text{Xe}$  ratios (where "mantle source" signifies that

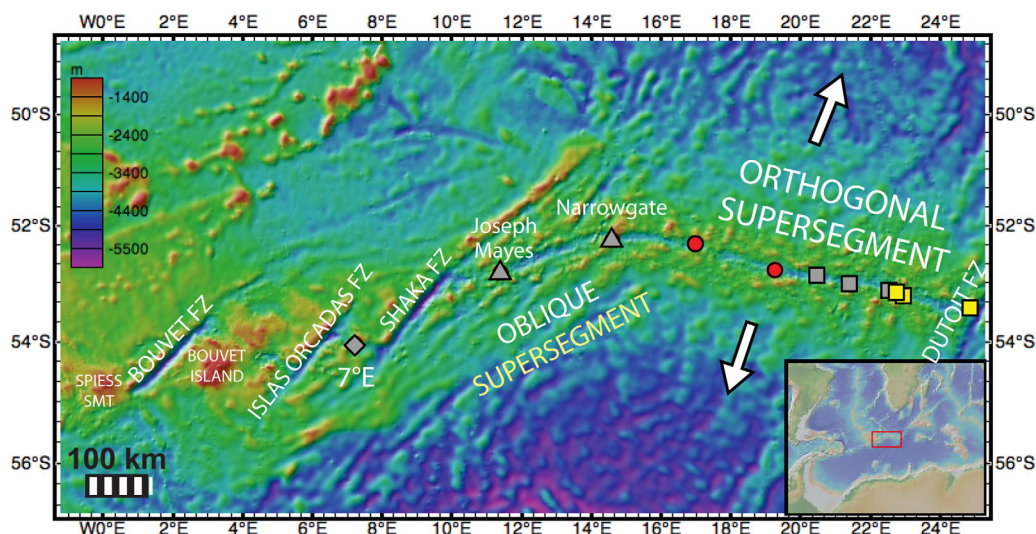


**Figure 1.** Map of the Southwest Indian Ridge study area. Symbols give locations of samples previously analyzed for He, CO<sub>2</sub>, Ne, Ar, and Xe compositions [Parai et al., 2012]. Red and yellow symbols represent the samples discussed here for Xe fission isotopes.

measured values are corrected for air contamination; see section 2.2) in an area removed from the influence of known plumes, and argued that these variations reflect heterogeneous incorporation of recycled atmospheric Ar and Xe (possibly associated with metasomatized subcontinental lithospheric mantle) into the SWIR Orthogonal Supersegment MORB mantle source. Here we investigate the integrated history of MORB source degassing and regassing evident in the Xe isotope systematics of SWIR Orthogonal Supersegment basalts. We discuss our new high-precision data and place them in context with an overview of I-Pu-U-Xe systematics in other MORB and plume-derived basalts. We find that MORB sources have experienced a greater extent of degassing than plume sources. Furthermore, we find that mantle source Xe budgets are dominated by recycled atmospheric Xe, indicating incorporation of trace-element depleted material even into sources with the most primitive Ne isotopes [e.g., Mukhopadhyay, 2012]. We thus harness the range of radiogenic, fissionogenic, and primordial isotopes of Xe in order to inform our understanding of the processes that have shaped the volatile budgets of the MORB and plume mantle reservoirs over Earth history.

## 2. Samples and Methods

Xenon isotopic compositions were determined for six MORB glass samples dredged from the Southwest Indian Ridge between 16°E and 25°E (Figure 1): four samples from the S.A. Agulhas expedition AG22 (AG22 1-1, AG22 1-4, AG22 9-2, and AG22 13-1) [Mahoney et al., 1992] and two samples from the R/V Knorr expedition KN162-7 (KN162-7 11–25 and KN162-7 22-14) [Dick et al., 2001]. Previous studies report sample details and have characterized the major element, trace element, and radiogenic lithophile isotopic compositions of these samples [Janney et al., 2005; Kurz et al., 1998; Mahoney et al., 1992; Standish, 2006; Standish et al., 2008], as well as their He, Ne, Ar, Xe, and CO<sub>2</sub> abundances and He, Ne, Ar, and Xe (<sup>129</sup>Xe/<sup>130</sup>Xe and <sup>136</sup>Xe/<sup>130</sup>Xe) isotopic compositions [Georgen et al., 2003; Parai et al., 2012; Standish, 2006]. In this study, we focus on the fission isotopes of Xe (<sup>131</sup>Xe, <sup>132</sup>Xe, <sup>134</sup>Xe, and <sup>136</sup>Xe) in samples removed from the influence of known mantle plumes. We divide the study area into two regions based on observed variations in <sup>40</sup>Ar/<sup>36</sup>Ar and <sup>129</sup>Xe/<sup>130</sup>Xe isotopic composition [Parai et al., 2012]: SWIR Western Orthogonal Supersegment (AG22 1-1, AG22 1-4, and KN162-7 11-25) and SWIR Eastern Orthogonal Supersegment (KN162-7 22-14, AG22 9-2, and AG22 13-1). We have noted previously that AG22 1-1 and 1-4 overlap in every isotope space [Parai et al., 2012]. These are rocks from a single dredge and are likely to sample a single flow; therefore, we consider them together as a single sample in all computations.

### 2.1. Sample Preparation and Mass Spectrometry

Samples were step-crushed under ultra-high vacuum using a hydraulic ram in order to release magmatic gases trapped in vesicles. One to five grams of the largest available glass chips (3–10 mm) were targeted for rare gas analysis, since the largest chips may host large intact vesicles. Analytical and mass spectrometric

methods have been previously presented [Parai *et al.*, 2012]. Procedural blanks were monitored during the step-crushing process. Xe blanks were typically ~2% of the measured sample  $^{130}\text{Xe}$  signal. Blanks were stable, low, and statistically indistinguishable from air in isotopic composition. All measured sample Xe isotope ratios reflect some degree of syn- to post-eruptive atmospheric contamination. Therefore, no blank corrections were made to the abundances or isotope ratios reported in Table 1. Each sample step-crush was bracketed by multiple air standard runs, which were used to calibrate sensitivity and mass discrimination as a function of signal size. A total of 1280 heavy noble gas air standard runs were analyzed over the 2 year SWIR analytical campaign, with signal sizes  $\sim 10^{-15}$  to  $10^{-13}$  cc STP  $^{130}\text{Xe}$ . Uncertainties in the Xe isotope ratios for each step-crush are based on the reproducibility of air standards of comparable signal size analyzed within the same time period (supporting information Figure S1).

### 2.2. Corrections for Syn- to Post-eruptive Atmospheric Contamination

Variable syn- to post-eruptive air contamination affects all measurements of Xe in mantle-derived rocks [e.g., Kunz *et al.*, 1998; Moreira *et al.*, 1998; Mukhopadhyay, 2012; Staudacher and Allegre, 1982; Trieloff and Kunz, 2005; Trieloff *et al.*, 2000]. Corrections for syn- to post-eruptive air contamination are required to accurately characterize the mantle source. If well-defined mixing arrays are observed, measured values can be modeled as two-component mixtures between the unknown mantle source isotopic composition and the known atmospheric composition. Well-defined mixing arrays in  $^{129}\text{Xe}/^{132}\text{Xe}$  -  $^{40}\text{Ar}/^{36}\text{Ar}$  space allow us to determine mantle source  $^{129}\text{Xe}/^{132}\text{Xe}$  composition by fitting and extrapolation to mantle source  $^{40}\text{Ar}/^{36}\text{Ar}$  values, which have been determined based on  $^{40}\text{Ar}/^{36}\text{Ar}$  -  $^{20}\text{Ne}/^{22}\text{Ne}$  systematics [Parai *et al.*, 2012]. The correction for atmospheric contamination is a total least squares hyperbolic extrapolation for mantle  $^{129}\text{Xe}/^{132}\text{Xe}$  (Figure 2 and supporting information Figure S2). Mantle source  $^{130}\text{Xe}/^{132}\text{Xe}$ ,  $^{131}\text{Xe}/^{132}\text{Xe}$ ,  $^{134}\text{Xe}/^{132}\text{Xe}$ , and  $^{136}\text{Xe}/^{132}\text{Xe}$  are determined by total least squares linear regression against  $^{129}\text{Xe}/^{132}\text{Xe}$  (supporting information Figures S3 and S4) and extrapolation to the mantle source  $^{129}\text{Xe}/^{132}\text{Xe}$  compositions. Correlated errors are taken into account after York [1969] and York *et al.* [2004]. Mantle source Xe isotopic compositions are reported in Table 2. We use  $^{132}\text{Xe}$  as the normalizing isotope:  $^{132}\text{Xe}$  is the most abundant isotope of Xe, and a relatively high signal in the normalizing isotope reduces the uncertainty in the measured isotopic ratio and minimizes the error correlation between isotope ratios. Additional considerations for the choice of normalizing isotope are discussed in section 2.3.1.

### 2.3. Linear Least Squares Determination of Initial, Recycled Atmospheric, Pu-Fissionogenic, and U-Fissionogenic Xe Components in the SWIR Mantle Source

The present-day  $^{131,132,134,136}\text{Xe}$  inventory in mantle sources can be modeled as a mixture of four components: (1) an initial Xe budget that is solar, chondritic, or U-Xe (a theoretical composition derived from meteorite data [Pepin, 2000]) in composition; (2) recycled atmospheric Xe; (3) Pu-fission Xe produced within the first ~500 Myr of Earth history and retained in the mantle; and (4) U-fission Xe retained in the mantle.  $^{244}\text{Pu}$  and  $^{238}\text{U}$  each produce fission  $^{131,132,134,136}\text{Xe}$  in characteristic proportions that are distinct from the  $^{131,132,134,136}\text{Xe}$  spectra in Earth's atmosphere and in primitive materials such as carbonaceous chondrites.

Accordingly, we may describe the Xe isotopic composition of the mantle source today with four equations of the form:

$$X_{init} \left( \frac{\zeta \text{Xe}}{^{132}\text{Xe}} \right)_{init} + X_{atm} \left( \frac{\zeta \text{Xe}}{^{132}\text{Xe}} \right)_{atm} + X_{Pu} \left( \frac{\zeta \text{Xe}}{^{132}\text{Xe}} \right)_{Pu} + X_U \left( \frac{\zeta \text{Xe}}{^{132}\text{Xe}} \right)_U = \left( \frac{\zeta \text{Xe}}{^{132}\text{Xe}} \right)_{mantle} \quad (1)$$

where  $\zeta = 130, 131, 134, \text{ and } 136$ ;  $x$  is the molar mixing proportion of  $^{132}\text{Xe}$ ; *init* designates the initial mantle composition, modeled here using either solar wind, average carbonaceous chondrite (AVCC), or U-Xe; *atm* designates recycled atmospheric Xe; *Pu* designates Pu-fission Xe; and *U* designates U-fission Xe. Component Xe isotopic spectra and references are given in Table 3. The  $^{132}\text{Xe}$  mixing proportions sum to 1:

$$X_{init} + X_{atm} + X_{Pu} + X_U = 1 \quad (2)$$

Therefore, we have five linear equations with four unknowns. We find the linear least squares solution to the system  $\mathbf{Ax} = \mathbf{b}$ , where  $\mathbf{A}$  is a matrix of mixing endmember isotopic compositions (Table 3),  $\mathbf{b}$  is a vector of mantle source Xe isotopic compositions, and  $\mathbf{x}$  is the best fit vector of  $^{132}\text{Xe}$  mixing proportions with the constraint that  $0 \leq x \leq 1$  for each component (see supporting information Text S1 for a detailed description of the computation).

**Table 1.** Southwest Indian Ridge 16°E-25°E Ar and Xe Abundances and Isotopic Compositions

Sample	Lat. (°S)	Long. (°E)	<sup>4</sup> He/ <sup>3</sup> He	Mass (g)	Step	×10 <sup>-11</sup> cc		×10 <sup>-14</sup> cc		<sup>129</sup> Xe/ <sup>132</sup> Xe		<sup>130</sup> Xe/ <sup>132</sup> Xe		<sup>131</sup> Xe/ <sup>132</sup> Xe		<sup>134</sup> Xe/ <sup>132</sup> Xe		<sup>136</sup> Xe/ <sup>132</sup> Xe		
						STP <sup>36</sup> Ar	STP <sup>130</sup> Xe	<sup>40</sup> Ar/ <sup>36</sup> Ar	1σ	1σ	1σ	1σ	1σ	1σ	1σ					
AG22 1-1	52.300	16.980	108000	2.933	1	6.8	1.1	3169	32	1.030	0.007	0.1522	0.0016	0.7803	0.0068	0.3991	0.0035	0.3453	0.0029	
					2	4.0	1.0	9243	92	1.074	0.007	0.1476	0.0015	0.7635	0.0066	0.4068	0.0035	0.3573	0.0029	
					3	67.5	8.4	766	8	0.996	0.002	0.1519	0.0006	0.7890	0.0025	0.3922	0.0011	0.3321	0.0010	
					4	7.6	1.7	2955	30	1.011	0.006	0.1511	0.0012	0.7879	0.0057	0.3970	0.0029	0.3393	0.0023	
					5	23.7	3.1	1205	12	0.998	0.004	0.1502	0.0007	0.7862	0.0042	0.3912	0.0021	0.3348	0.0016	
					6	1.2	0.3	9847	98	1.091	0.013	0.1518	0.0027	0.7842	0.0112	0.4113	0.0062	0.3590	0.0052	
					7	5.8	1.0	3896	39	1.043	0.008	0.1507	0.0017	0.7745	0.0070	0.4001	0.0037	0.3486	0.0030	
					8	1.6	0.5	12520	130	1.054	0.011	0.1439	0.0022	0.7588	0.0095	0.4069	0.0053	0.3584	0.0045	
					9	2.9	1.0	7000	70	1.021	0.007	0.1519	0.0017	0.7808	0.0071	0.3997	0.0037	0.3441	0.0030	
					10	0.8	0.3	13100	130	1.050	0.012	0.1521	0.0027	0.7914	0.0114	0.4085	0.0062	0.3506	0.0051	
					11	1.8	0.4	4714	47	1.031	0.012	0.1506	0.0026	0.7814	0.0108	0.4012	0.0058	0.3454	0.0048	
					1.926	1	21.3	3.4	1559	16	1.001	0.003	0.1504	0.0008	0.7882	0.0035	0.3917	0.0016	0.3348	0.0014
					2	14.8	2.2	2086	21	1.008	0.005	0.1506	0.0009	0.7894	0.0053	0.3940	0.0027	0.3393	0.0020	
					3	2.6	0.7	10090	100	1.074	0.009	0.1474	0.0019	0.7678	0.0080	0.4100	0.0044	0.3577	0.0037	
					4	4.3	0.9	5857	59	1.043	0.008	0.1515	0.0018	0.7780	0.0074	0.4031	0.0039	0.3548	0.0033	
					5	1.7	0.5	11740	120	1.060	0.011	0.1474	0.0023	0.7783	0.0098	0.4109	0.0054	0.3610	0.0046	
					6	8.3	1.2	1703	17	1.013	0.006	0.1514	0.0015	0.7794	0.0062	0.3974	0.0032	0.3382	0.0026	
					7	1.0	0.3	7729	77	1.049	0.013	0.1535	0.0029	0.7787	0.0116	0.4147	0.0065	0.3551	0.0054	
					1.310	1	17.0	1.5	3275	33	1.036	0.007	0.1508	0.0010	0.7874	0.0035	0.3988	0.0019	0.3468	0.0016
					2	18.7	2.4	3612	36	1.035	0.007	0.1499	0.0008	0.7810	0.0034	0.4038	0.0021	0.3460	0.0020	
3	1.6	0.4	9643	96	1.057	0.011	0.1499	0.0039	0.7784	0.0110	0.4076	0.0078	0.3553	0.0053						
4	1.3	0.4	9317	93	1.060	0.011	0.1455	0.0039	0.7925	0.0114	0.3993	0.0079	0.3478	0.0054						
AG22 1-4	52.300	16.980	2.998	1	33.3	4.6	1269	13	0.999	0.003	0.1504	0.0007	0.7820	0.0031	0.3933	0.0014	0.3349	0.0013		
				2	7.5	2.4	3906	39	1.013	0.005	0.1506	0.0009	0.7808	0.0052	0.3982	0.0027	0.3396	0.0020		
				3	16.6	3.3	2105	21	1.000	0.003	0.1508	0.0008	0.7794	0.0036	0.3946	0.0017	0.3372	0.0014		
				4	2.1	0.6	12490	120	1.084	0.010	0.1505	0.0021	0.7780	0.0088	0.4193	0.0049	0.3655	0.0041		
				5	4.0	0.9	6786	68	1.055	0.008	0.1478	0.0017	0.7745	0.0073	0.4071	0.0039	0.3528	0.0032		
				6	2.1	0.5	12180	120	1.074	0.011	0.1477	0.0022	0.7644	0.0092	0.4139	0.0052	0.3632	0.0044		
				7	5.2	0.9	4285	43	1.028	0.008	0.1490	0.0017	0.7757	0.0074	0.3990	0.0039	0.3461	0.0032		
				8	1.0	0.4	15340	150	1.086	0.012	0.1508	0.0026	0.7707	0.0108	0.4110	0.0061	0.3627	0.0051		
				9	1.7	0.3	5848	58	1.044	0.012	0.1473	0.0027	0.7868	0.0113	0.4035	0.0061	0.3505	0.0051		
KN162-7 11-25	52.799	19.200	104000	4.064	1	3.7	1.6	6886	69	1.022	0.006	0.1535	0.0013	0.7947	0.0049	0.3912	0.0027	0.3356	0.0021	
					2	86.1	11.1	877	9	0.993	0.003	0.1512	0.0006	0.7856	0.0023	0.3887	0.0011	0.3326	0.0008	
					3	1.2	0.5	26650	270	1.115	0.013	0.1450	0.0026	0.7604	0.0113	0.4138	0.0060	0.3701	0.0044	
					4	2.7	1.2	27240	270	1.111	0.007	0.1462	0.0013	0.7704	0.0049	0.4274	0.0031	0.3697	0.0024	
					5	0.7	0.4	27610	280	1.084	0.014	0.1490	0.0030	0.7650	0.0131	0.4026	0.0066	0.3596	0.0048	
					6	2.3	2.4	20120	200	1.091	0.005	0.1487	0.0010	0.7755	0.0039	0.4119	0.0021	0.3646	0.0017	
					7	5.6	2.0	16490	160	1.091	0.006	0.1475	0.0011	0.7763	0.0042	0.4142	0.0024	0.3610	0.0019	
					8	2.5	1.1	18610	190	1.082	0.007	0.1504	0.0014	0.7813	0.0052	0.4125	0.0032	0.3621	0.0025	
					9	1.8	0.8	26780	270	1.116	0.009	0.1491	0.0018	0.7719	0.0067	0.4229	0.0040	0.3670	0.0031	
					10	3.7	1.9	28500	290	1.114	0.006	0.1482	0.0011	0.7677	0.0041	0.4189	0.0024	0.3726	0.0019	
					11	3.5	1.2	13390	130	1.080	0.007	0.1469	0.0014	0.7808	0.0051	0.4121	0.0031	0.3613	0.0025	
					12	1.0	0.4	21960	220	1.091	0.014	0.1448	0.0027	0.7671	0.0121	0.4189	0.0065	0.3580	0.0045	
2.488	1	96.8	43.9	647	6	0.986	0.002	0.1505	0.0005	0.7844	0.0019	0.3890	0.0007	0.3315	0.0005					
2	4.0	3.0	14660	150	1.090	0.004	0.1477	0.0009	0.7758	0.0039	0.4128	0.0019	0.3634	0.0016						
3	4.3	1.6	10840	110	1.033	0.006	0.1489	0.0013	0.7671	0.0047	0.4021	0.0028	0.3434	0.0022						
4	0.5	0.1	5955	60	1.051	0.016	0.1509	0.0035	0.8163	0.0163	0.4234	0.0080	0.3493	0.0052						
KN162-7 22-14	53.109	22.647	102000	3.024	1	4.9	1.4	6488	65	1.037	0.006	0.1477	0.0014	0.7765	0.0050	0.4028	0.0030	0.3500	0.0023	
					2	10.1	3.2	8492	85	1.037	0.004	0.1497	0.0009	0.7775	0.0039	0.4021	0.0018	0.3494	0.0015	
					3	4.7	2.7	15610	160	1.050	0.005	0.1486	0.0010	0.7798	0.0039	0.4039	0.0020	0.3531	0.0016	
					4	5.2	2.5	14550	150	1.053	0.005	0.1482	0.0010	0.7773	0.0039	0.4070	0.0021	0.3527	0.0016	
					5	14.3	3.8	7665	77	1.048	0.004	0.1495	0.0008	0.7756	0.0035	0.4047	0.0017	0.3494	0.0014	
					6	4.6	4.5	11940	120	1.044	0.004	0.1482	0.0008	0.7780	0.0032	0.4031	0.0016	0.3531	0.0014	
					7	3.5	3.6	14050	140	1.051	0.004	0.1488	0.0008	0.7797	0.0036	0.4069	0.0018	0.3554	0.0015	
					8	2.3	2.9	17540	180	1.063	0.004	0.1494	0.0009	0.7786	0.0040	0.4109	0.0019	0.3546	0.0015	
					9	1.1	0.8	20700	210	1.056	0.009	0.1518	0.0020	0.7870	0.0077	0.4062	0.0042	0.3533	0.0032	
AG22 9-2	53.130	22.880	99500	3.921	1	47.2	8.8	1584	16	1.003	0.003	0.1502	0.0006	0.7848	0.0023	0.3929	0.0013	0.3353	0.0011	
					2	18.4	4.7	3840	38	1.032	0.004	0.1494	0.0007	0.7844	0.0028	0.4004	0.0018	0.3447	0.0014	
					3	4.7	2.8	8991	90	1.037	0.005	0.1508	0.0010	0.7876	0.0044	0.4022	0.0018	0.3479	0.0015	
					4	5.6	1.9	6109	61	1.048	0.007	0.1503	0.0013	0.7867	0.0056	0.4063	0.0021	0.3478	0.0020	
					5	7.1	2.7	6579	66	1.029	0.005	0.1489	0.0010	0.7812	0.0043	0.3977	0.0018	0.3439	0.0014	
					6	6.0	1.9	5614	56	1.046	0.006	0.1504	0.0013	0.7846	0.0056	0.4035	0.0020	0.3478	0.0020	
					7	1.8	0.7	8279	83	1.049	0.012	0.1505	0.0022	0.7818	0.0097	0.4070	0.0035	0.3459	0.0033	
					8	1.8	0.8	9537	95	1.041	0.011	0.1504	0.0021	0.7853	0.0092	0.4046	0.0035	0.3486	0.0033	

Table 1. (continued)

Sample	Lat. (°S)	Long. (°E)	<sup>4</sup> He/ <sup>3</sup> He	Mass (g)	Step	×10 <sup>-11</sup> cc		×10 <sup>-14</sup> cc		<sup>129</sup> Xe/ <sup>132</sup> Xe		<sup>130</sup> Xe/ <sup>132</sup> Xe		<sup>131</sup> Xe/ <sup>132</sup> Xe		<sup>134</sup> Xe/ <sup>132</sup> Xe		<sup>136</sup> Xe/ <sup>132</sup> Xe	
						STP <sup>36</sup> Ar	STP <sup>130</sup> Xe	<sup>40</sup> Ar/ <sup>36</sup> Ar	1σ	1σ	1σ	1σ	1σ	1σ	1σ	1σ			
AG22 13-1	53.408	24.758	99000	4.600	9	1.6	0.6	7883	79	1.033	0.014	0.1475	0.0024	0.7705	0.0113	0.3995	0.0037	0.3468	0.0034
					10	0.6	0.2	8648	115	1.021	0.019	0.1466	0.0032	0.7636	0.0165	0.3937	0.0043	0.3409	0.0038
					1	14.1	2.5	3579	36	1.023	0.005	0.1479	0.0010	0.7831	0.0039	0.4024	0.0021	0.3475	0.0016
					2	9.5	3.0	8286	83	1.053	0.004	0.1504	0.0009	0.7816	0.0040	0.4073	0.0019	0.3527	0.0015
					3	40.7	12.4	1259	13	1.004	0.003	0.1515	0.0005	0.7854	0.0022	0.3924	0.0010	0.3360	0.0007
					4	73.1	9.3	904	9	0.990	0.003	0.1498	0.0006	0.7808	0.0024	0.3894	0.0012	0.3325	0.0009
					5	102.0	12.5	670	7	0.991	0.003	0.1516	0.0005	0.7853	0.0022	0.3889	0.0010	0.3318	0.0007
					6	52.1	6.3	1434	14	1.006	0.003	0.1511	0.0007	0.7845	0.0027	0.3945	0.0015	0.3368	0.0012
					7	95.0	12.0	760	8	0.992	0.003	0.1511	0.0005	0.7852	0.0022	0.3915	0.0010	0.3332	0.0007
					8	30.2	4.5	1844	18	1.014	0.004	0.1507	0.0008	0.7787	0.0033	0.3960	0.0016	0.3389	0.0013
					9	11.8	3.0	5028	50	1.034	0.004	0.1494	0.0009	0.7811	0.0040	0.4000	0.0019	0.3496	0.0015
					10	18.5	3.9	3707	37	1.023	0.004	0.1505	0.0008	0.7820	0.0035	0.4009	0.0017	0.3459	0.0014
					11	55.4	6.9	1317	13	0.999	0.003	0.1497	0.0006	0.7803	0.0026	0.3924	0.0014	0.3335	0.0011
12	6.4	1.6	6347	63	1.048	0.006	0.1505	0.0013	0.7830	0.0047	0.4066	0.0028	0.3528	0.0021					
13	66.4	8.8	1116	11	0.999	0.003	0.1508	0.0006	0.7822	0.0025	0.3913	0.0013	0.3341	0.0010					

Sample eruption depths are reported in Parai et al. (2012).

Based on our solutions for the mixing proportions of initial Xe, recycled atmospheric Xe, Pu-fission Xe, and U-fission Xe, we compute the ratios  $^{136}\text{Xe}_{\text{Pu}} / (^{136}\text{Xe}_{\text{Pu}} + ^{136}\text{Xe}_{\text{U}})$  and  $^{129}\text{Xe}^* / ^{136}\text{Xe}_{\text{Pu}}$ :

$$^{136}\text{Xe}_{\text{Pu}} = [^{132}\text{Xe}] \cdot x_{\text{Pu}} \left( \frac{^{136}\text{Xe}}{^{132}\text{Xe}} \right)_{\text{Pu}} \quad (3)$$

$$^{136}\text{Xe}_{\text{U}} = [^{132}\text{Xe}] \cdot x_{\text{U}} \left( \frac{^{136}\text{Xe}}{^{132}\text{Xe}} \right)_{\text{U}} \quad (4)$$

$$\left[ \frac{^{136}\text{Xe}_{\text{Pu}}}{^{136}\text{Xe}_{\text{Pu}} + ^{136}\text{Xe}_{\text{U}}} \right] = \left[ \frac{x_{\text{Pu}} \left( \frac{^{136}\text{Xe}}{^{132}\text{Xe}} \right)_{\text{Pu}}}{x_{\text{Pu}} \left( \frac{^{136}\text{Xe}}{^{132}\text{Xe}} \right)_{\text{Pu}} + x_{\text{U}} \left( \frac{^{136}\text{Xe}}{^{132}\text{Xe}} \right)_{\text{U}}} \right] \quad (5)$$

$$^{129}\text{Xe}^* = [^{132}\text{Xe}] \cdot \left[ \left( \frac{^{129}\text{Xe}}{^{132}\text{Xe}} \right)_{\text{mantle}} - x_{\text{init}} \left( \frac{^{129}\text{Xe}}{^{132}\text{Xe}} \right)_{\text{init}} - x_{\text{atm}} \left( \frac{^{129}\text{Xe}}{^{132}\text{Xe}} \right)_{\text{atm}} \right] \quad (6)$$

$$\left( \frac{^{129}\text{Xe}^*}{^{136}\text{Xe}_{\text{Pu}}} \right) = \left[ \frac{\left( \frac{^{129}\text{Xe}}{^{132}\text{Xe}} \right)_{\text{mantle}} - \left[ x_{\text{init}} \left( \frac{^{129}\text{Xe}}{^{132}\text{Xe}} \right)_{\text{init}} + x_{\text{atm}} \left( \frac{^{129}\text{Xe}}{^{132}\text{Xe}} \right)_{\text{atm}} \right]}{x_{\text{Pu}} \left( \frac{^{136}\text{Xe}}{^{132}\text{Xe}} \right)_{\text{Pu}}} \right] \quad (7)$$

where  $[^{132}\text{Xe}]$  denotes the concentration of  $^{132}\text{Xe}$ ; we note that the ratios are not dependent on  $[^{132}\text{Xe}]$ .

The uncertainties in the mixing proportions of  $^{132}\text{Xe}$  are determined by Monte Carlo error propagation. Values for the vector of mantle source compositions  $\mathbf{b}$  are randomly drawn from a population distributed normally around the best mantle source values with a dispersion given by the 1 sigma uncertainties reported in Table 4. Based on  $10^6$  random drawings of  $\mathbf{b}$ , we collect statistics on the  $10^6$  corresponding solution vectors,  $\mathbf{x}$ , and on the distributions of resulting ratios  $^{136}\text{Xe}_{\text{Pu}} / (^{136}\text{Xe}_{\text{Pu}} + ^{136}\text{Xe}_{\text{U}})$  and  $^{129}\text{Xe}^* / ^{136}\text{Xe}_{\text{Pu}}$ .

### 2.3.1. Choice of $^{132}\text{Xe}$ as the Normalizing Isotope for Linear Least Squares Optimizations

The mixing proportions of initial mantle, recycled atmospheric, Pu-fission, and U-fission Xe that make up the present-day mantle source Xe are determined using isotope ratios with  $^{132}\text{Xe}$  as the normalizing isotope, rather than the less abundant but nonfissionogenic  $^{130}\text{Xe}$ . We emphasize that our calculation simply models the present-day mantle composition as a linear mixture of four distinct compositions, none of which varies through time (in reality, the atmospheric Xe composition does evolve for at least the first Gyr of Earth history; see section 2.3.2). The mantle source Xe composition moves through Xe isotope space over time: it starts at the initial mantle Xe composition and moves on a path that reflects fissionogenic ingrowth (following vectors toward fixed compositions for Pu-fission and U-fission) and an increasing proportion of recycled atmospheric Xe, until it reaches the present-day mantle Xe composition. Our calculation simply apportions

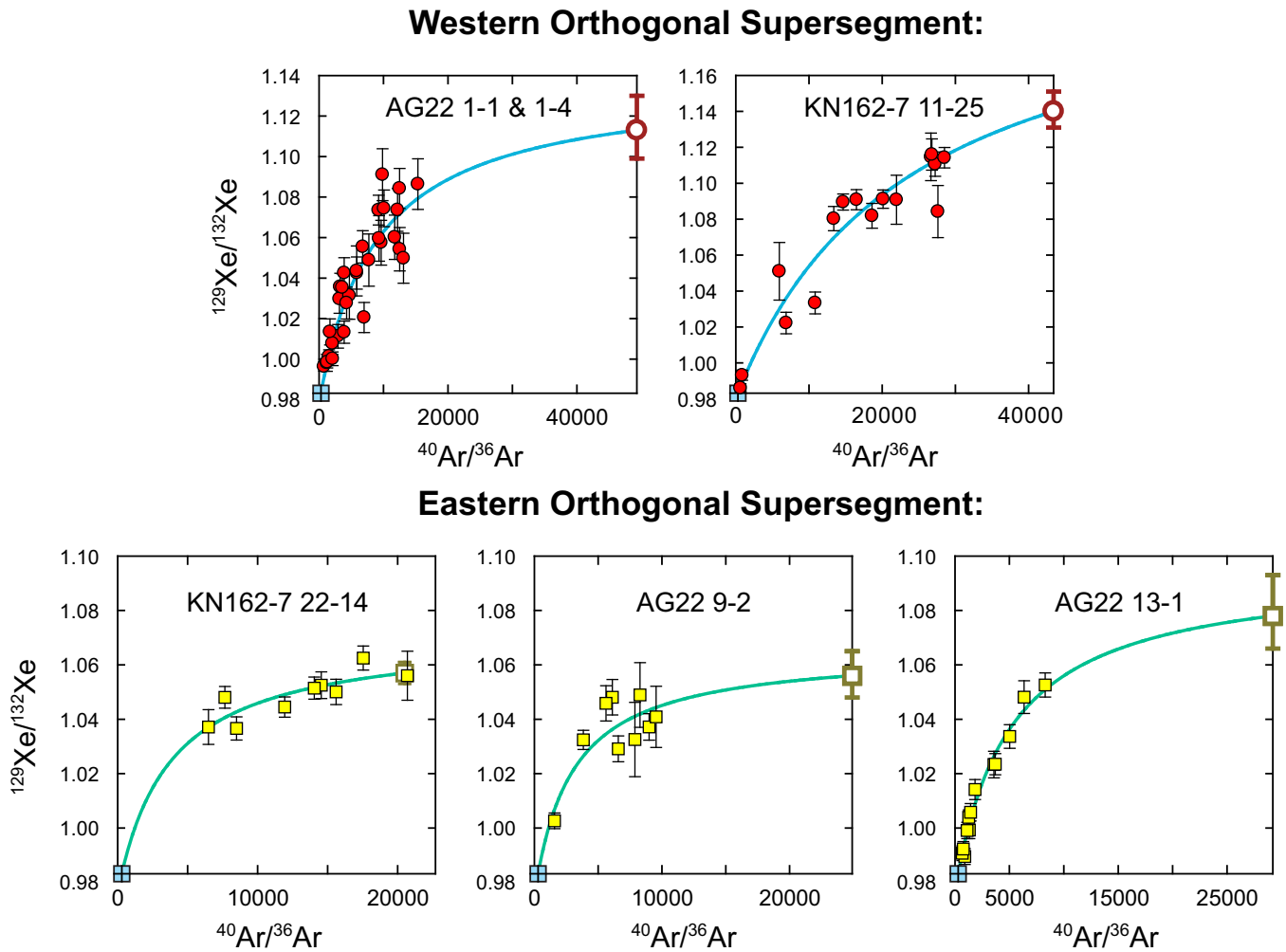


**Figure 2.** Correction for syn- to post-eruptive atmospheric contamination to determine mantle source  $^{129}\text{Xe}/^{132}\text{Xe}$ . For each sample, step-crushing generates an array reflecting variable degrees of atmospheric contamination. For samples with well-defined hyperbolic mixing arrays in  $^{129}\text{Xe}/^{132}\text{Xe} - ^{40}\text{Ar}/^{36}\text{Ar}$  space, best fit hyperbolae yield extrapolated mantle source  $^{129}\text{Xe}/^{132}\text{Xe}$  (bold open symbols) at mantle source  $^{40}\text{Ar}/^{36}\text{Ar}$  values determined previously [Parai *et al.*, 2012]. We note that for Eastern Orthogonal Supersegment samples, the extrapolation is not very sensitive to the mantle  $^{40}\text{Ar}/^{36}\text{Ar}$  as best fit hyperbolae asymptote with respect to the x axis at  $^{129}\text{Xe}/^{132}\text{Xe}$  values of  $\sim 1.06$  to  $1.08$ . In contrast, measured values in Western Orthogonal Supersegment sample reach  $^{129}\text{Xe}/^{132}\text{Xe}$  values of  $\sim 1.12$ .

the present-day mantle Xe budget to these four constituent components. In this sense, the time-integrated contributions to  $^{132}\text{Xe}$  from Pu-fission and U-fission are equivalent to contributions to  $^{130}\text{Xe}$  from initial mantle and recycled atmosphere; there is no reason to avoid normalization to either isotope. However, normalization to  $^{130}\text{Xe}$  presents a difficulty in that fissionogenic  $^{130}\text{Xe}$  is negligible, and  $^{130}\text{Xe}$ -normalized Pu-fission and U-fission isotope ratios go to infinity. It is not possible to find least squares solutions when infinite terms are introduced into the linear mixing expression (equation (1)), and so  $^{130}\text{Xe}$  is not a viable normalization candidate for the purposes of this calculation. We note that our computations are directly analogous to familiar lever-rule solutions for two-component mixing of oxygen in  $^{17}\text{O}/^{16}\text{O}$  versus  $^{18}\text{O}/^{16}\text{O}$  space, where two components with distinct  $^{16}\text{O}$ - $^{17}\text{O}$ - $^{18}\text{O}$  spectra mix linearly.

### 2.3.2. Evolution of the Atmospheric Xe Isotopic Composition Over Earth History

Studies of ancient atmospheric gases trapped in Archean cherts formed at  $\sim 3.5$  Gyr show that the Xe isotopic composition of the Archean atmosphere differed from the present-day atmosphere [e.g., Pujol *et al.*, 2011]. This suggests that isotopically fractionating loss of Xe occurred over a period that extended at least 1 billion years into Earth history, and that the atmosphere evolved in isotopic composition until it reached its present-day composition at some time after 3.5 Gyr. If recycling of atmospheric Xe into the mantle occurred early in Earth history, then the isotopic composition of recycled atmospheric Xe has accordingly evolved over time. Since both the Xe recycling rate over time and the precise time-evolution of the atmospheric Xe

**Table 2.** SWIR Mantle Source Xe Isotopic Compositions

Sample	$^{129}\text{Xe}/^{132}\text{Xe}$	+1 $\sigma$	-1 $\sigma$	$^{130}\text{Xe}/^{132}\text{Xe}$	1 $\sigma$	$^{131}\text{Xe}/^{132}\text{Xe}$	1 $\sigma$	$^{134}\text{Xe}/^{132}\text{Xe}$	1 $\sigma$	$^{136}\text{Xe}/^{132}\text{Xe}$	1 $\sigma$
AG22 1-1 and 1-4	1.113	0.017	0.014	0.1474	0.0009	0.7580	0.0041	0.4225	0.0023	0.3739	0.0021
KN162-7 11-25	1.140	0.011	0.009	0.1466	0.0006	0.7671	0.0022	0.4262	0.0014	0.3786	0.0012
KN162-7 22-14	1.057	0.004	0.004	0.1486	0.0004	0.7769	0.0016	0.4075	0.0008	0.3553	0.0008
AG22 9-2	1.056	0.009	0.008	0.1492	0.0006	0.7818	0.0024	0.4067	0.0012	0.3519	0.0012
AG22 13-1	1.078	0.015	0.012	0.1488	0.0007	0.7701	0.0029	0.4143	0.0015	0.3634	0.0015
Average SWIR West	1.127	0.014	0.014	0.1470	0.0005	0.7664	0.0019	0.4237	0.0011	0.3754	0.0010
Average SWIR East	1.064	0.007	0.007	0.1487	0.0003	0.7761	0.0012	0.4095	0.0007	0.3572	0.0006

isotopic composition are poorly constrained, we do not attempt to incorporate this evolution into our model. However, we note a number of physical reasons that the bulk recycled atmospheric Xe composition is likely to reflect modern atmospheric Xe. First, a higher Archean mantle potential temperature should promote shallow release of atmospheric fluids from any downwelling assemblages in the early Earth and should thus inhibit early Xe recycling to the deep Earth. The flux of recycled atmospheric Xe should increase as the Earth cools and the retention of atmospheric fluids within subducting slabs beyond depths of magma generation becomes more favorable. Furthermore, since the mantle turnover time scale is estimated to be between a few hundreds of Myr and ~1 Gyr [e.g., *Coltice et al., 2009; Donnelly et al., 2004; Gonnemann and Mukhopadhyay, 2009; Iwamori et al., 2010*], the mantle recycled atmospheric Xe budget should be primarily composed of Xe subducted after ~2.5 Ga, at which point the atmosphere approaches the modern Xe composition [*Pujol et al., 2011*]. Therefore, even if ancient atmospheric Xe were recycled efficiently to the mantle early in Earth history, the recycled atmospheric Xe budget of the mantle should still be dominated by the modern atmospheric Xe composition. Lastly, we find that if we perform the least squares optimizations using the ~3.5 Ga Archean chert Xe composition [*Pujol et al., 2011*] for the composition of recycled atmospheric Xe, we achieve poor fits with residuals an order of magnitude larger than achieved with the modern atmospheric Xe composition. Therefore, we present our results using the modern atmospheric composition for recycled atmospheric Xe in our linear least squares computations.

### 3. Results

The SWIR mantle source  $^{129}\text{Xe}/^{132}\text{Xe}$  and  $^{130,131,134,136}\text{Xe}/^{132}\text{Xe}$  compositions (corrected for syn- to post-eruptive atmospheric contamination) are shown in Figure 2 and supporting information Figures S3 and S4, respectively, and reported in Table 2. The linear least squares solutions for mixing proportions of  $^{132}\text{Xe}$  are reported in Table 4 and illustrated in Figure 3 and supporting information Figures S5 and S6. Mixing proportion results for Equatorial Atlantic depleted MORB [*Tucker et al., 2012*] and plume-derived samples from Iceland [*Mukhopadhyay, 2012*] and the Rochambeau Rift [*Petö et al., 2013*] are also shown in Figures 3, S5, and S6 for comparison. The medians and 68% confidence intervals for the  $^{129}\text{Xe}^*/^{136}\text{Xe}_{\text{Pu}}, ^{136}\text{Xe}_{\text{Pu}}/(^{136}\text{Xe}_{\text{Pu}} + ^{136}\text{Xe}_{\text{U}})$  and fraction of  $^{132}\text{Xe}$  from recycled atmospheric Xe for the SWIR Western and Eastern Orthogonal Supersegments are shown in Figures 4–6, along with results for Equatorial Atlantic depleted MORBs [*Tucker et al., 2012*]. Continental well gases sample noble gases derived from the upper mantle [*Caffee et al., 1999; Holland and Ballentine, 2006; Staudacher, 1987*]. However, well gas Xe also reflects contributions from both crustal U-fission and shallow atmospheric contamination, and we cannot simultaneously

**Table 3.** Xenon Endmember Compositions

	$^{130}\text{Xe}/^{132}\text{Xe}$	$^{131}\text{Xe}/^{132}\text{Xe}$	$^{134}\text{Xe}/^{132}\text{Xe}$	$^{136}\text{Xe}/^{132}\text{Xe}$
Atmosphere <sup>a</sup>	0.1513	0.7895	0.3880	0.3296
Solar wind <sup>b</sup>	0.1661	0.8272	0.3666	0.2985
AVCC <sup>c</sup>	0.1626	0.8200	0.3836	0.3233
U-Xe <sup>d</sup>	0.1654	0.8262	0.3516	0.2740
Pu-fission <sup>e</sup>	0	0.2777	1.0413	1.1198
U-fission <sup>f</sup>	0	0.1449	1.4370	1.7375

<sup>a</sup>*Basford et al. [1973].*

<sup>b</sup>*Wieler and Baur [1994] and Pepin et al. [1995].*

<sup>c</sup>*Pepin [1991, 2000].*

<sup>d</sup>*Pepin [2000] and Pepin and Porcelli [2002].*

<sup>e</sup>Error-weighted average of data from *Alexander et al. [1971], Lewis [1975], and Hudson et al. [1989].*

<sup>f</sup>Error-weighted average of data from *Wetherill [1953], Hebeda et al. [1987], Eikenberg et al. [1993], and Ragetti et al. [1994].*

**Table 4.** Linear Least Squares Solutions for Mixing Proportions of  $^{132}\text{Xe}^a$

		Initial Mantle								
		AVCC			Solar Wind			U-Xe		
		Median	+1 $\sigma$	-1 $\sigma$	Median	+1 $\sigma$	-1 $\sigma$	Median	+1 $\sigma$	-1 $\sigma$
SWIR Western Orthogonal Supersegment	Initial mantle	0.110	0.069	0.063	0.155	0.061	0.061	0.186	0.060	0.060
	Recycled atmosphere	0.850	0.068	0.074	0.799	0.067	0.066	0.767	0.065	0.065
	Pu-fission	0.014	0.011	0.011	0.022	0.010	0.011	0.016	0.007	0.007
	U-fission	0.025	0.006	0.006	0.024	0.005	0.005	0.031	0.003	0.003
	$^{129}\text{Xe}^*/^{136}\text{Xe}_{\text{Pu}}$	10.8	39.4	4.8	7.3	6.6	2.3	9.8	7.6	2.9
SWIR Eastern Orthogonal Supersegment	Initial mantle	0.27	0.20	0.21	0.37	0.15	0.17	0.25	0.09	0.10
	Recycled atmosphere	0.083	0.040	0.040	0.096	0.036	0.036	0.107	0.036	0.035
	Pu-fission	0.892	0.043	0.043	0.877	0.039	0.039	0.865	0.038	0.039
	U-fission	0.011	0.007	0.007	0.013	0.006	0.006	0.009	0.004	0.004
	$^{129}\text{Xe}^*/^{136}\text{Xe}_{\text{Pu}}$	0.014	0.004	0.004	0.015	0.003	0.003	0.019	0.002	0.002
Equatorial Atlantic Depleted Mantle [Tucker et al., 2012]	Initial mantle	8.3	14.6	3.2	7.1	6.4	2.3	10.6	10.7	3.5
	Recycled atmosphere	0.32	0.19	0.20	0.36	0.15	0.16	0.22	0.09	0.11
	Pu-fission	0.071	0.064	0.064	0.084	0.058	0.058	0.091	0.057	0.057
	U-fission	0.883	0.069	0.069	0.868	0.064	0.064	0.861	0.062	0.062
	$^{129}\text{Xe}^*/^{136}\text{Xe}_{\text{Pu}}$	0.019	0.011	0.010	0.022	0.010	0.010	0.017	0.007	0.007
Bravo Dome Well Gas [Holland and Ballentine, 2006]	Initial mantle	0.026	0.005	0.006	0.027	0.005	0.005	0.031	0.002	0.002
	Total atmosphere (recycled + shallow)	8.1	8.3	2.9	7.3	6.2	2.3	9.0	5.7	2.5
	Pu-fission	0.32	0.17	0.16	0.34	0.14	0.15	0.27	0.09	0.10
	U-fission	0.095	0.037	0.037	0.086	0.033	0.032	0.082	0.032	0.027
	$^{129}\text{Xe}^*/^{136}\text{Xe}_{\text{Pu}}$	0.878	0.040	0.040	0.886	0.035	0.036	0.891	0.029	0.035
Harding County Well Gas [Caffee et al., 1999]	Initial mantle	0.017	0.003	0.003	0.020	0.003	0.003	0.024	0.001	0.001
	Total atmosphere (recycled + shallow)	0.010	0.006	0.006	0.009	0.006	0.006	0.004	0.004	0.004
	Pu-fission	8.8	14.0	3.3	10.2	16.8	3.9	24.1	872	12.2
	U-fission	0.27	0.16	0.16	0.23	0.01	0.14	0.09	0.01	0.09
	$^{129}\text{Xe}^*/^{136}\text{Xe}_{\text{Pu}}$	0.119	0.016	0.016	0.115	0.015	0.015	0.114	0.015	0.015
Rochambeau Rift—NLD27 [Petö et al., 2013]	Initial mantle	0.852	0.017	0.017	0.854	0.016	0.016	0.857	0.016	0.016
	Recycled atmosphere	0.011	0.003	0.003	0.010	0.003	0.003	0.003	0.002	0.002
	Pu-fission	0.018	0.002	0.002	0.020	0.001	0.001	0.026	0.001	0.001
	U-fission	7.7	2.5	1.5	8.8	2.8	1.7	29.6	39.4	10.7
	$^{129}\text{Xe}^*/^{136}\text{Xe}_{\text{Pu}}$	0.28	0.07	0.07	0.24	0.05	0.06	0.07	0.04	0.04
Iceland—DICE [Mukhopadhyay, 2012]	Initial mantle	0.110	0.011	0.027	0.136	0.016	0.023	0.163	0.027	0.028
	Recycled atmosphere	0.869	0.030	0.012	0.839	0.025	0.017	0.811	0.030	0.029
	Pu-fission	0.020	0.001	0.005	0.025	0.001	0.005	0.020	0.003	0.003
	U-fission	0.001	0.003	0.001	0.001	0.002	0.000	0.007	0.001	0.001
	$^{129}\text{Xe}^*/^{136}\text{Xe}_{\text{Pu}}$	2.9	1.0	0.2	2.6	0.5	0.1	3.3	0.6	0.4
MORB Average	Initial mantle	0.95	0.04	0.23	0.97	0.03	0.14	0.65	0.07	0.08
	Recycled atmosphere	0.065	0.012	0.022	0.023	0.042	0.023	0	0.023	0
	Pu-fission	0.915	0.024	0.012	0.959	0.025	0.047	0.984	0.001	0.025
	U-fission	0.020	0.001	0.004	0.013	0.008	0.004	0.010	0.003	0.001
	$^{129}\text{Xe}^*/^{136}\text{Xe}_{\text{Pu}}$	0.0001	0.003	0	0.005	0.002	0.004	0.006	0.001	0.001
Plume-Influenced Average <sup>d</sup>	Initial mantle	2.8	0.7	0.1	4.4	2.0	1.6	5.9	1.0	1.2
	Recycled atmosphere	0.99	0.01	0.19	0.65	0.31	0.19	0.50	0.10	0.08
	Pu-fission	8.2	2.0	1.3	8.4	1.8	1.2	9.7	3.2	1.9
MORB Average	U-fission	0.31	0.11	0.11	0.36	0.09	0.09	0.25	0.05	0.06
	$^{129}\text{Xe}^*/^{136}\text{Xe}_{\text{Pu}}$	2.9	0.4	0.1	2.6	2.7	0.2	3.7	1.0	0.6
Plume-Influenced Average <sup>d</sup>	U-fission	0.97	0.02	0.11	0.96	0.03	0.43	0.60	0.07	0.07
	$^{136}\text{Xe}_{\text{Pu}}/(^{136}\text{Xe}_{\text{Pu}} + ^{136}\text{Xe}_{\text{U}})$									

<sup>a</sup>+1 $\sigma$  and -1 $\sigma$  give 68% confidence limits.

<sup>b</sup>This study, Tucker et al. [2012], Caffee et al. [1999], and Holland and Ballentine [2006]. Well gases not included in MORB average with U-Xe as initial mantle (supporting information S2).

<sup>c</sup>This study, Tucker et al. [2012]. Well gases not included (supporting information S2).

<sup>d</sup>Mukhopadhyay [2012] and Petö et al. [2013].

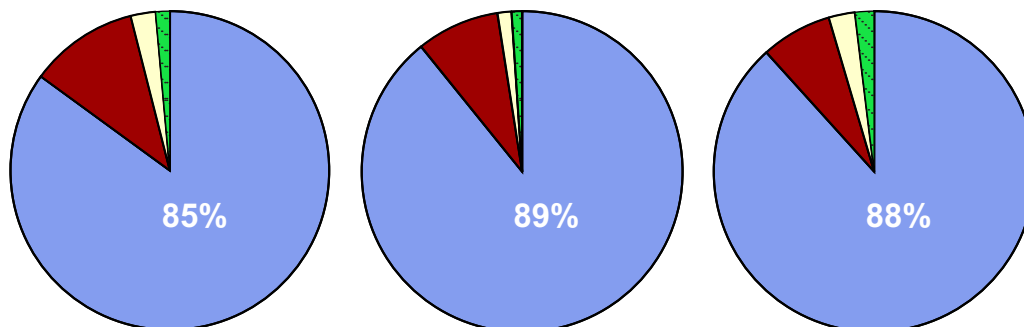
correct for these contaminants to determine the well gas mantle source Xe composition. We emphasize that well gas mixing proportion results are therefore not directly comparable to results from basalts: we obtain well gas Xe mixing proportions for the initial mantle Xe, the total atmospheric Xe contribution (both recycled and shallow-level contamination), Pu-fission Xe and total U-fission Xe (from both the mantle source and the continental crust that hosts the well gas). Based on these computations, we are able to estimate the mantle source  $^{129}\text{Xe}^*/^{136}\text{Xe}_{\text{Pu}}$ , and we include the median and 68% confidence interval for  $^{129}\text{Xe}^*/^{136}\text{Xe}_{\text{Pu}}$  in well gases in Figure 4 (see supporting information S2). Results for plume-influenced samples from Iceland [Mukhopadhyay, 2012] and the Rochambeau Rift [Petö et al., 2013] are also shown for comparison in Figures 4–6.

**Mid-ocean ridge basalts:**

SWIR Western OSS

SWIR Eastern OSS

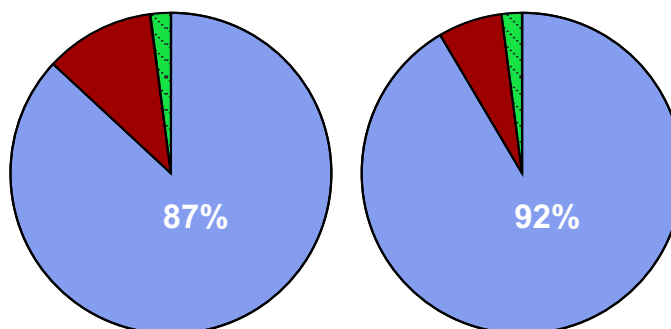
Equatorial Atlantic DM



**Plume-influenced basalts:**

Rochambeau Rift

Iceland



**Fraction <sup>132</sup>Xe from:**

- recycled atm Xe
- initial Xe (AVCC)
- U-fission Xe
- Pu-fission Xe

**Figure 3.** Pie charts illustrating the median proportions of present-day mantle <sup>132</sup>Xe derived from recycled atmosphere, initial mantle (AVCC shown here; see supporting information Figures S5 and S6 for solar wind and U-Xe results), U-fission and Pu-fission in SWIR Western and Eastern Orthogonal Supersegment mantle sources. Results for Equatorial Atlantic depleted MORB [Tucker et al., 2012], Rochambeau Rift [Petó et al., 2013], and Iceland [Mukhopadhyay, 2012] mantle sources are shown for comparison. Recycled atmospheric Xe uniformly dominates the mantle Xe budget (percentages given in white). Fission Xe in the mantle sources of plume-influenced basalts is primarily derived from Pu-fission.

We emphasize that it is unlikely that any single sample location can be taken as representative of the bulk MORB source or plume source. For example, the SWIR Orthogonal Supersegment mantle source incorporates an enriched component (possibly metasomatized subcontinental lithospheric mantle) [Hart, 1984; Hawkesworth et al., 1986; Mahoney et al., 1992], and its Xe isotopic composition may differ from a hypothetical depleted MORB endmember Xe composition. However, instead of searching for a single sample to represent the depleted endmember mantle composition, we aim to characterize as many MORB and plume sources as possible in order to gain a fuller portrait of mantle heterogeneity. We therefore examine both individual locations and group averages to investigate whether broad differences in MORB and plume Xe isotope systematics exist. Our results indicate that mantle source <sup>132</sup>Xe budgets are uniformly dominated by the recycled atmospheric component (Figures 3 and 6). A median value of 85% of the <sup>132</sup>Xe in the SWIR Western Orthogonal Supersegment mantle source and 89% of the <sup>132</sup>Xe in the SWIR Eastern Orthogonal Supersegment mantle source is recycled atmospheric Xe (using AVCC as the initial mantle Xe). Similarly, 88% of the <sup>132</sup>Xe in the Equatorial Atlantic depleted MORB source is recycled atmospheric Xe [Tucker et al., 2012]. Samples from sources influenced by mantle plumes have 87% (Rochambeau Rift) [Petó et al., 2013] and 92% (Iceland) [Mukhopadhyay, 2012] of <sup>132</sup>Xe derived from recycled atmosphere. Thus, even in sources with the most primitive Ne isotopic compositions, more than 85% of the Xe is recycled atmospheric Xe (Figure 6).

<sup>129</sup>Xe\*/<sup>136</sup>Xe<sub>Pu</sub> in the SWIR mantle sources are  $11 \pm_{-4.8}^{+39}$  (68% confidence intervals) for SWIR Western Orthogonal Supersegment and  $8.3 \pm_{-3.2}^{+14.6}$  for SWIR Eastern Orthogonal Supersegment using AVCC for the initial mantle Xe (Table 4; Figures 3 and 4). These ratios are consistent with values of  $8.1 \pm_{-2.9}^{+8.3}$  computed for Equatorial Atlantic depleted MORBs [Tucker et al., 2012],  $7.7 \pm_{-1.5}^{+2.5}$  for Harding County well gas [Caffee et al., 1999],

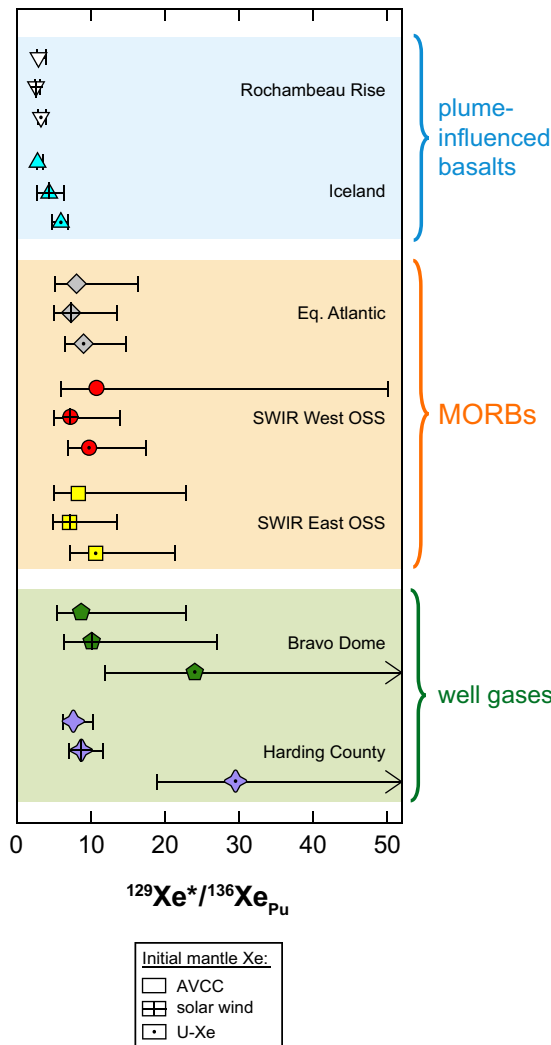


**Figure 4.** Medians and 68% confidence intervals determined by Monte Carlo error propagation for  $^{129}\text{Xe}^*/^{136}\text{Xe}_{\text{Pu}}$  are shown for SWIR Western Orthogonal Supersegment, SWIR Eastern Orthogonal Supersegment, and Equatorial Atlantic [Tucker et al., 2012] MORB sources. Results for Bravo Dome [Holland and Ballentine, 2006] and Harding County [Caffee et al., 1999] well gas and for mantle sources of plume-influenced basalts from the Rochambeau Rift [Petó et al., 2013] and Iceland [Mukhopadhyay, 2012] are shown for comparison. Results using AVCC (open symbols), solar wind (crossed symbols), and U-Xe (dotted symbols) for the initial mantle Xe are indicated. Regardless of the choice of initial mantle Xe (AVCC, solar wind, or U-Xe), mantle sources of plume-influenced basalts are uniformly characterized by lower  $^{129}\text{Xe}^*/^{136}\text{Xe}_{\text{Pu}}$  values (medians range from ~2.5 to 6) relative to MORB sources (medians range from ~7 to 11).

( $^{136}\text{Xe}_{\text{Pu}} + ^{136}\text{Xe}_{\text{U}}$ ) values between  $0.05 \pm 0.05$  and  $0.32 \pm 0.09$ , where the variation reflects the differences in the method employed to correct the shallow-level air contamination. Unfortunately, we cannot make a self-consistent comparison between our data and the Kunz et al. [1998] data set as  $^{132}\text{Xe}$ -normalized fission Xe isotopes are not available. Therefore, we derive an error-weighted MORB average  $^{136}\text{Xe}_{\text{Pu}} / (^{136}\text{Xe}_{\text{Pu}} + ^{136}\text{Xe}_{\text{U}})$  of  $0.31 \pm 0.11$  and  $0.36 \pm 0.09$  based only on the SWIR and the Equatorial Atlantic data (Figure 7b) for AVCC and solar wind as the initial mantle Xe, respectively.

$^{136}\text{Xe}_{\text{Pu}} / (^{136}\text{Xe}_{\text{Pu}} + ^{136}\text{Xe}_{\text{U}})$  values in plume-influenced mantle sources are  $0.95^{+0.04}_{-0.23}$  for Rochambeau Rift [Petó et al., 2013] and  $0.99^{+0.01}_{-0.19}$  for Iceland [Mukhopadhyay, 2012], giving a plume-influenced mantle error-weighted

and  $8.8^{+14.0}_{-3.3}$  for Bravo Dome well gas [Holland and Ballentine, 2006]. We use SWIR Western and Eastern Orthogonal Supersegment  $^{129}\text{Xe}^*/^{136}\text{Xe}_{\text{Pu}}$  values together with Equatorial Atlantic depleted MORB, Harding County well gas, and Bravo Dome well gas  $^{129}\text{Xe}^*/^{136}\text{Xe}_{\text{Pu}}$  to compute an error-weighted average value for the MORB source of  $8.2^{+2.0}_{-1.3}$  with AVCC as the initial mantle Xe (Table 4 and Figure 7a). Using solar wind as the initial mantle Xe,  $^{129}\text{Xe}^*/^{136}\text{Xe}_{\text{Pu}}$  values of  $7.3^{+6.6}_{-2.3}$ ,  $7.1^{+6.4}_{-2.3}$ ,  $7.3^{+6.2}_{-2.3}$ ,  $8.8^{+2.8}_{-1.7}$ , and  $10^{+17}_{-3.9}$  are computed for the SWIR Western Orthogonal Supersegment, SWIR Eastern Orthogonal Supersegment, Equatorial Atlantic depleted MORBs, Harding County well gas, and Bravo Dome well gas, respectively, giving an error-weighted MORB average  $^{129}\text{Xe}^*/^{136}\text{Xe}_{\text{Pu}}$  of  $8.4^{+1.8}_{-1.2}$  (Table 4 and Figure 7a). These estimates agree within error, indicating computed  $^{129}\text{Xe}^*/^{136}\text{Xe}_{\text{Pu}}$  values are not strongly dependent on the choice of the mantle initial Xe component (Figures 4 and 7).

$^{136}\text{Xe}_{\text{Pu}} / (^{136}\text{Xe}_{\text{Pu}} + ^{136}\text{Xe}_{\text{U}})$  in the SWIR mantle sources are  $0.27^{+0.20}_{-0.21}$  for the SWIR Western Orthogonal Supersegment and  $0.32^{+0.19}_{-0.20}$  for the SWIR Eastern Orthogonal Supersegment, using AVCC for the initial mantle Xe (Table 4 and Figure 5). These ratios are consistent with values of  $0.32^{+0.17}_{-0.16}$  computed for Equatorial Atlantic depleted MORBs [Tucker et al., 2012]. Kunz et al. [1998] reported  $^{130}\text{Xe}$ -normalized fission Xe isotopes for the gas-rich mid-North Atlantic popping rock and determined a  $^{136}\text{Xe}_{\text{Pu}} / (^{136}\text{Xe}_{\text{Pu}} + ^{136}\text{Xe}_{\text{U}})$  ratio of  $0.32 \pm 0.1$  using modern atmosphere as the initial mantle Xe. However, using solar wind as the initial Xe and a small subset of the popping rock data, Pepin and Porcelli [2006] estimated a very high  $^{136}\text{Xe}_{\text{Pu}} / (^{136}\text{Xe}_{\text{Pu}} + ^{136}\text{Xe}_{\text{U}})$  ratio of  $0.75^{+0.11}_{-0.21}$ . Using the entire popping rock data set and solar wind as the initial Xe, Mukhopadhyay [2012] derived  $^{136}\text{Xe}_{\text{Pu}} /$

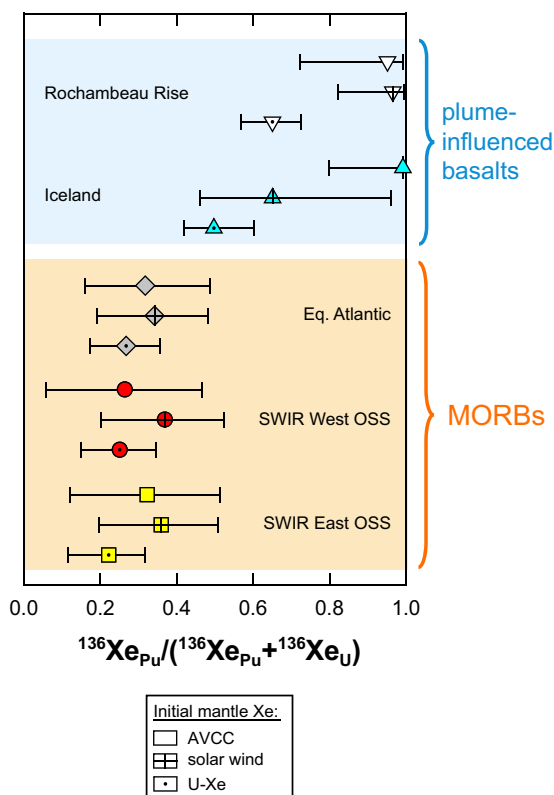


**Figure 5.** Medians and 68% confidence intervals determined by Monte Carlo error propagation for the fraction of fission Xe derived from Pu-fission,  $^{136}\text{Xe}_{\text{Pu}} / (^{136}\text{Xe}_{\text{Pu}} + ^{136}\text{Xe}_{\text{U}})$ , are shown for SWIR Western Orthogonal Supersegment, SWIR Eastern Orthogonal Supersegment, and Equatorial Atlantic [Tucker et al., 2012] MORB sources. Results for mantle sources of plume-influenced basalts from the Rochambeau Rift [Petö et al., 2013] and Iceland [Mukhopadhyay, 2012] are shown for comparison. Symbols as in Figure 4. Regardless of the choice of initial mantle Xe (AVCC, solar wind, or U-Xe), mantle sources of plume-influenced basalts are uniformly characterized by higher  $^{136}\text{Xe}_{\text{Pu}} / (^{136}\text{Xe}_{\text{Pu}} + ^{136}\text{Xe}_{\text{U}})$  values (medians range from  $\sim 0.49$  to 1.0) relative to MORB sources (medians range from  $\sim 0.22$  to 0.36).

noble gases into the deep mantle [e.g., Staudacher and Allegre, 1988]. However, recent work indicates that atmospheric heavy noble gases are carried in subducted materials beyond depths of magma generation to be recycled into the mantle [e.g., Holland and Ballentine, 2006; Kendrick et al., 2011; Mukhopadhyay, 2012; Parai et al., 2012; Petö et al., 2013; Tucker et al., 2012]. Having explicitly corrected for syn- to post-eruptive atmospheric contamination, here we evaluate the prevalence of atmospheric Xe incorporation into mantle sources. We find that  $\sim 80$ – $95\%$  of the  $^{132}\text{Xe}$  budget of MORB and plume mantle sources is recycled atmospheric Xe (Table 4; Figures 3, 6, S5, and S6). Our result is broadly consistent with estimates based on well gas primordial Xe isotope systematics that find up to  $\sim 80\%$  of  $^{130}\text{Xe}$  in the well gas mantle source is derived from recycled atmospheric Xe [Holland and Ballentine, 2006]. The dominance of recycled atmospheric Xe indicates that recycled material is incorporated into both MORB and plume sources. However, while atmospheric Xe is recycled into the plume source [Holland and Ballentine, 2006; Mukhopadhyay, 2012; Petö et al., 2013], differential incorporation of atmospheric Xe [Holland and Ballentine, 2006] cannot explain observed differences in  $^{129}\text{Xe}/^{130}\text{Xe}$  between MORB and plume sources [Mukhopadhyay, 2012; Petö et al., 2013]. Rather,  $^{129}\text{Xe} - ^{136}\text{Xe} - ^{130}\text{Xe}$  systematics illustrate that MORB and plume sources (1) are not related by mixing with the atmosphere; (2) separated within 100 Ma of the start of the Solar System; and (3) have not been homogenized by 4.45 Ga of mantle convection [Mukhopadhyay, 2012; Tucker et al., 2012; Parai et al., 2012; Petö et al., 2013].

average of  $0.97^{+0.02}_{-0.11}$  using AVCC as the initial mantle Xe (Table 4). Computed  $^{136}\text{Xe}_{\text{Pu}} / (^{136}\text{Xe}_{\text{Pu}} + ^{136}\text{Xe}_{\text{U}})$  values are relatively insensitive to the choice of mantle initial Xe component (Figures 5 and 7b). We note that MORB source  $^{136}\text{Xe}_{\text{Pu}} / (^{136}\text{Xe}_{\text{Pu}} + ^{136}\text{Xe}_{\text{U}})$  ratios are consistently lower than plume source values.

## 4. Discussion

Xenon fission isotope systematics in the SWIR mantle source contribute to an emerging portrait of a MORB mantle that has experienced heterogeneous degassing and regassing on a variety of length scales and time scales. Below we discuss our determinations of SWIR mantle fission Xe in the context of results for other MORB sources and plume-influenced sources. We find that Xe fission isotopes indicate both significant regassing of atmospheric Xe into the MORB and plume mantle sources, as well as different degrees of degassing for the MORB and plume reservoirs over Earth history. High-precision xenon isotopic measurements thus provide unique insights into the volatile evolution histories of mantle sources.

### 4.1. Recycling of Atmospheric Xe into MORB and Plume Sources: Evidence for Incorporation of Recycled Material into Mantle Reservoirs

Subduction zones were long thought to be efficient barriers to the recycling of

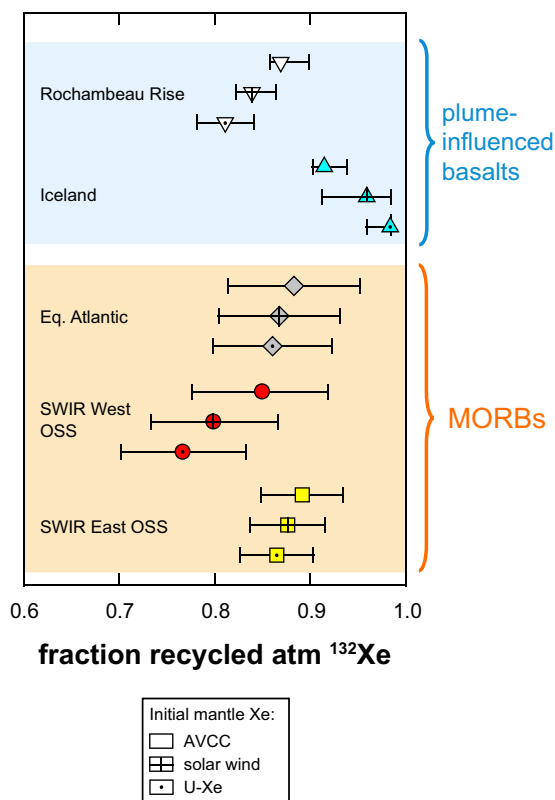


**Figure 6.** Medians and 68% confidence intervals determined by Monte Carlo error propagation for the proportion of mantle  $^{132}\text{Xe}$  derived from recycled atmosphere are shown for SWIR Western Orthogonal Supersegment, SWIR Eastern Orthogonal Supersegment, and Equatorial Atlantic [Tucker *et al.*, 2012] MORB sources. Results for mantle sources of plume-influenced basalts from the Rochambeau Rift [Petö *et al.*, 2013] and Iceland [Mukhopadhyay, 2012] are shown for comparison. Symbols as in Figure 4. Recycled atmospheric Xe dominates the present-day mantle Xe budget. We note that regardless of the choice of initial mantle Xe (AVCC, solar wind, or U-Xe), the Eastern Orthogonal Supersegment consistently exhibits a higher proportion of recycled atmospheric Xe relative to the Western Orthogonal Supersegment. This observation supports the interpretation that large variations in SWIR Orthogonal Supersegment  $^{40}\text{Ar}/^{36}\text{Ar}$  and  $^{129}\text{Xe}/^{130}\text{Xe}$  reflect heterogeneous incorporation of recycled atmospheric heavy noble gases [Parai *et al.*, 2012].

an indication of nonchondritic bulk silicate Earth [e.g., Jackson *et al.*, 2010; Jackson and Jellinek, 2013], but may rather arise from incorporation of depleted recycled material into primordial sources [e.g., Gonnermann and Mukhopadhyay, 2009].

#### 4.2. MORB and Plume Sources Have Experienced Different Degassing Histories

Mantle  $^{136}\text{Xe}_{\text{Pu}}/(^{136}\text{Xe}_{\text{Pu}} + ^{136}\text{Xe}_{\text{U}})$  ratios provide constraints on the long-term degassing histories of mantle sources.  $^{244}\text{Pu}$  decays with a half-life of 80.0 Myr; production of Pu-fission  $^{136}\text{Xe}_{\text{Pu}}$  is effectively complete at  $\sim 500$  Myr. In contrast,  $^{238}\text{U}$  decays with a half-life of 4.468 Gyr and production of U-fission  $^{136}\text{Xe}_{\text{U}}$  is ongoing. In order to preserve a high  $^{136}\text{Xe}_{\text{Pu}}/(^{136}\text{Xe}_{\text{Pu}} + ^{136}\text{Xe}_{\text{U}})$  ratio, a mantle source must retain a high proportion of the Pu-fission  $^{136}\text{Xe}_{\text{Pu}}$  budget developed in the first 500 Myr of Earth history. A mantle source that experiences significant degassing loses both  $^{136}\text{Xe}_{\text{Pu}}$  and  $^{136}\text{Xe}_{\text{U}}$ , but only grows  $^{136}\text{Xe}_{\text{U}}$  back over time. Thus, a relatively degassed mantle source develops a low  $^{136}\text{Xe}_{\text{Pu}}/(^{136}\text{Xe}_{\text{Pu}} + ^{136}\text{Xe}_{\text{U}})$  ratio over time.

We find that MORB mantle sources uniformly exhibit a low  $^{136}\text{Xe}_{\text{Pu}}/(^{136}\text{Xe}_{\text{Pu}} + ^{136}\text{Xe}_{\text{U}})$  ratio relative to plume-related sources (Figures 5 and 8) [Mukhopadhyay, 2012; Tucker *et al.*, 2012; Petö *et al.*, 2013]. Median MORB source  $^{136}\text{Xe}_{\text{Pu}}/(^{136}\text{Xe}_{\text{Pu}} + ^{136}\text{Xe}_{\text{U}})$  ratios range from 0.27 to 0.37, with an error-weighted average of  $0.28^{+0.11}_{-0.10}$  using AVCC as the mantle initial Xe; median plume-related source  $^{136}\text{Xe}_{\text{Pu}}/(^{136}\text{Xe}_{\text{Pu}} + ^{136}\text{Xe}_{\text{U}})$  ratios range from 0.65 to 0.97, with an error-weighted average of  $0.96^{+0.03}_{-0.18}$  using AVCC as the mantle initial

Among noble gases, Xe isotope systematics are particularly well suited to track the injection and incorporation of recycled atmospheric components into the mantle. Due to low overall concentrations of He and Ne (either atmospheric, radiogenic, or nucleogenic) in recycled material relative to ambient mantle material, the presence of recycled material does not always manifest clearly in a radiogenic He or nucleogenic Ne isotope signature in the mantle source [e.g., Parai *et al.*, 2009]. For example, although  $\sim 90\%$  of Iceland Xe is recycled in origin [Mukhopadhyay, 2012], Iceland Ne isotopes are primitive and near-solar, indicating incorporation of recycled material with high Xe/Ne into the Iceland source. Thus, plume-related samples with primitive He and Ne isotopic compositions may not reflect sampling of an undiluted primordial mantle. As a result, major and trace element compositions of samples with primitive He and Ne [e.g., Jackson *et al.*, 2010; Jackson and Jellinek, 2013] are unlikely to represent the composition of pristine primordial bulk silicate Earth. We note that the incorporation of recycled material generates depleted  $^{143}\text{Nd}/^{144}\text{Nd}$  ratios over time in both the upper mantle and the plume source: if continental crust with low Sm/Nd is built via extraction processes at subduction zones, then the average recycled slab package (i.e., crust and mantle lithosphere) over Earth history must have high Sm/Nd relative to the bulk silicate Earth. Therefore, the association of primitive He and Ne with superchondritic  $^{143}\text{Nd}/^{144}\text{Nd}$  isotopes is not

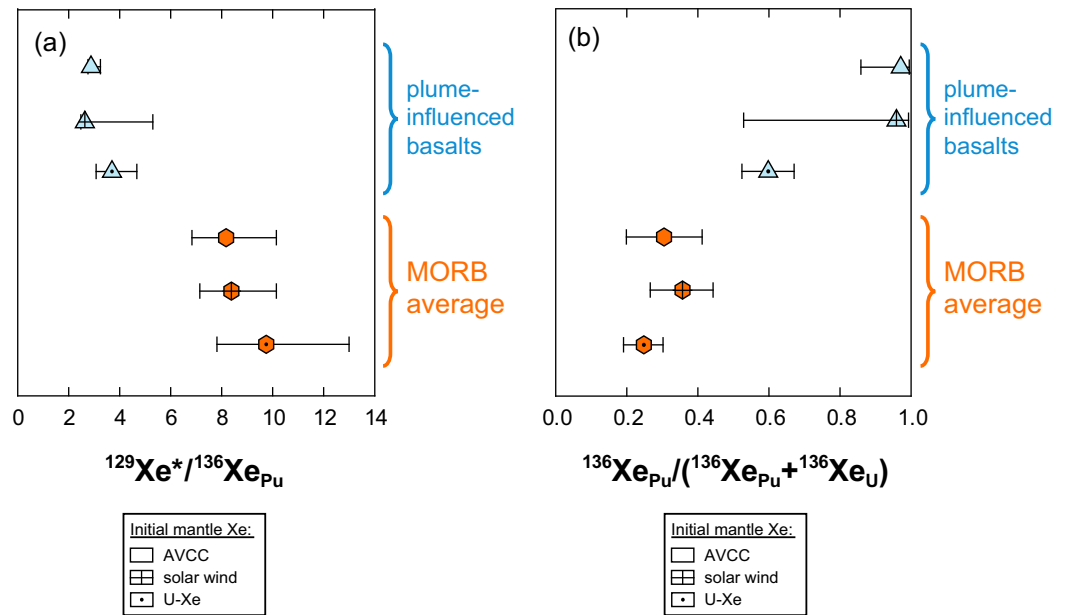


**Figure 7.** Error-weighted averages for (a) the ratio of iodine-derived to plutonium-derived Xe ( $^{129}\text{Xe}^*/^{136}\text{Xe}_{\text{Pu}}$ ) and (b) the fraction of fission Xe derived from Pu fission ( $^{136}\text{Xe}_{\text{Pu}}/(^{136}\text{Xe}_{\text{Pu}} + ^{136}\text{Xe}_{\text{U}})$ ) in MORB sources [Tucker *et al.*, 2012; this study] and the sources of plume-influenced basalts [Mukhopadhyay, 2012; Petö *et al.*, 2013]. Well gas data are included for the MORB average for  $^{129}\text{Xe}^*/^{136}\text{Xe}_{\text{Pu}}$ , except in the case where the initial mantle is U-Xe (see supporting information S2). Error bars indicate 68% confidence intervals. Regardless of the choice of initial mantle Xe (AVCC, solar wind, or U-Xe), mantle sources of plume-influenced basalts are uniformly characterized by lower  $^{129}\text{Xe}^*/^{136}\text{Xe}_{\text{Pu}}$  and higher  $^{136}\text{Xe}_{\text{Pu}}/(^{136}\text{Xe}_{\text{Pu}} + ^{136}\text{Xe}_{\text{U}})$  values relative to MORB sources.

Xe. The observed difference in  $^{136}\text{Xe}_{\text{Pu}}/(^{136}\text{Xe}_{\text{Pu}} + ^{136}\text{Xe}_{\text{U}})$  indicates that MORB mantle sources have uniformly experienced a greater extent of integrated degassing associated with long-term mantle processing relative to plume sources. We note that this observation is independent of the interpretation of  $^4\text{He}/^3\text{He}$  systematics in MORBs and plume-derived basalts.

### 4.3. The Emerging Portrait of Distinct Ancient, Heterogeneous and Continuously Evolving Mantle Sources

Xenon isotopic data from the Southwest Indian Ridge [Parai *et al.*, 2012; this study] add to a growing pool of high-precision fission Xe data in mid-ocean ridge basalts [Kunz *et al.*, 1998; Tucker *et al.*, 2012] and plume-influenced basalts [Mukhopadhyay, 2012; Petö *et al.*, 2013]. We find that the origin of the reservoir supplying primordial noble gases to plumes is fundamentally distinct from that of the MORB mantle reservoir: the two reservoirs cannot be related simply by differential degassing or incorporation of recycled atmospheric volatiles [Mukhopadhyay, 2012; Parai *et al.*, 2012; Petö *et al.*, 2013; Tucker *et al.*, 2012]. Based on the extinct  $^{129}\text{I}$ - $^{129}\text{Xe}$  system, some of the noble gases in plumes are supplied by a source that separated from the MORB source within 100 Myr of the start of the Solar System, and this ancient reservoir has not been destroyed and homogenized with the rest of the mantle by 4.45 Gyr of convection [Mukhopadhyay, 2012; Parai *et al.*, 2012; Petö *et al.*, 2013; Tucker *et al.*, 2012]. Furthermore, the distinct low  $^{129}\text{Xe}^*/^{136}\text{Xe}_{\text{Pu}}$  signature in plumes (Figures 4 and 7a) likely signifies that the ancient source sampled by plumes is characterized by a lower I/Pu than the MORB source [cf. Ozima *et al.*, 1985], and may reflect heterogeneous accretion, with early accretion being volatile-poor. Lastly, distinct MORB and plume source  $^3\text{He}/^{22}\text{Ne}$  ratios likely reflect ancient differences in degassing during the giant impact and magma ocean stage of early Earth history [Tucker and Mukhopadhyay, 2014]. Thus, noble gas data in mantle-derived basalts reflect very ancient differences that persist in the MORB and plume mantle reservoirs today.

Although differences between the upper mantle and plume source cannot be explained by recycling of atmospheric volatiles, injection, and incorporation of atmospheric heavy noble gases (Ar, Kr, Xe) into the mantle must occur over Earth history. Large variations are evident in upper mantle  $^{40}\text{Ar}/^{36}\text{Ar}$  and  $^{129}\text{Xe}/^{130}\text{Xe}$  isotopic composition in regions of the Southwest Indian Ridge removed from the influence of known mantle plumes, indicating heterogeneous incorporation of recycled atmospheric noble gases into

the MORB source [Parai *et al.*, 2012]. Our evaluation of SWIR fission Xe isotopes (section 3; Figure 6) supports this conclusion, as recycled atmospheric Xe constitutes ~87–90% of the  $^{132}\text{Xe}$  budget in the Eastern Orthogonal Supersegment mantle source and 77–85% of the  $^{132}\text{Xe}$  budget in the Western Orthogonal Supersegment source (Figure 6, see caption). The persistence of large Ar and Xe isotopic variations generated by heterogeneous regassing reflects inefficient homogenization of recycled material in the MORB mantle source.

We note that mantle source He and Ne isotopic compositions may not be sensitive to incorporation of recycled material due to low overall concentrations of He and Ne in recycled material relative to ambient mantle (section 4.1). Thus, the broad homogeneity noted in MORB helium isotopic compositions does not indicate a homogeneous MORB source [Graham, 2002; Graham *et al.*, 1992; Kurz *et al.*, 1982a, 1982b]. Based on Ar and Xe isotopic compositions measured in mantle-derived samples, we propose that MORB and plume source heterogeneities reflect the ongoing incorporation of recycled material into distinct ancient mantle reservoirs.

## 5. Conclusions

We present new high-precision measurements of the fission isotopes of Xe ( $^{131}\text{Xe}$ ,  $^{132}\text{Xe}$ ,  $^{134}\text{Xe}$ , and  $^{136}\text{Xe}$ ) in basalts from the Southwest Indian Ridge between 16°E and 25°E. Based on determinations of the mantle source isotopic compositions corrected for syn- to post-eruptive atmospheric contamination, we solve for the proportions of mantle  $^{132}\text{Xe}$  attributed to the primordial mantle Xe budget, recycling of atmospheric Xe, fission of extinct  $^{244}\text{Pu}$ , and ongoing fission of extant  $^{238}\text{U}$ .

We find that recycled atmospheric Xe dominates the Xe inventories of the SWIR Western and Eastern Orthogonal Supersegment mantle sources (~80–90% of  $^{132}\text{Xe}$  is recycled in origin), consistent with results from recent studies of Equatorial Atlantic MORBs [Tucker *et al.*, 2012] and plume-influenced basalts from Iceland [Mukhopadhyay, 2012] and the Rochambeau Rift [Pető *et al.*, 2013]. We assert that superchondritic  $^{143}\text{Nd}/^{144}\text{Nd}$  isotopes in mantle sources with primitive He and Ne do not necessitate a nonchondritic bulk silicate Earth; rather, the prevalence of recycled atmospheric Xe in these sources indicates the incorporation of depleted recycled material into primitive mantle sources. While significant regassing of the mantle is evident, we also find differences in the extent of degassing of the MORB and plume sources. MORB sources are consistently characterized by a lower fraction of fission Xe derived from Pu-fission, indicating a greater extent of degassing relative to the plume source. Therefore, our Southwest Indian Ridge Xe isotopic data contribute to an emerging portrait of two ancient mantle sources with distinct histories of early outgassing, processing via partial melting, and incorporation of recycled material in association with plate tectonics.

## Acknowledgments

The data supporting all results in this paper are given in Tables 1–4. We thank David Graham and an anonymous reviewer for comments that helped to improve the paper. We thank the Woods Hole Oceanographic Institution for providing samples for this study. This work was supported by NSF EAR 1450659 and OCE 0929193.

## References

- Alexander, E. C., R. S. Lewis, J. H. Reynolds and M. C. Michel (1971), Plutonium-244—Confirmation as an extinct radioactivity, *Science*, 172(3985), 837–840.
- Basford, J. R., J. C. Dragon, R. O. Pepin, M. R. Coscio Jr. and V. R. Murthy (1973), Krypton and xenon in lunar fines, *Proc. Lunar Sci. Conf. 4th*, *Geochim. Cosmochim. Acta*, 2, suppl., 1915–1955.
- Boulos, M. S., and O. K. Manuel (1971), Xenon record of extinct radioactivities in Earth, *Science*, 174, 1334.
- Caffee, M. W., G. B. Hudson, C. Velsko, G. R. Huss, E. C. Alexander Jr., and A. R. Chivas (1999), Primordial noble gases from Earth's mantle: Identification of a primitive volatile component, *Science*, 285, 2115–2118.
- Class, C., and S. L. Goldstein (2005), Evolution of helium isotopes in the Earth's mantle, *Nature*, 436, 1107–1112.
- Coltice, N., B. Marty, and R. Yokochi (2009), Xenon isotope constraints on the thermal evolution of the early Earth, *Chem. Geol.*, 266, 4–9.
- Dick, H. J. B., J. Lin, and H. Schouten (2001), An investigation of the effects of ridge geometry on crustal accretion at ultra-slow spreading rates: The SW Indian Ridge from 9° to 23.5° E, KN 162 Legs VII and IV Cruise Report, Woods Hole Oceanographic Inst., Woods Hole, Massachusetts.
- Donnelly, K. E., S. L. Goldstein, C. H. Langmuir, and M. Spiegelman (2004), Origin of enriched ocean ridge basalts and implications for mantle dynamics, *Earth Planet. Sci. Lett.*, 226, 347–366.
- Eikenberg, J., P. Signer, and R. Wieler (1993), U-Xe, U-Kr, and U-Pb systematics for dating uranium minerals and investigations of the production of nucleogenic neon and argon, *Geochim. Cosmochim. Acta*, 57(5), 1053–1069.
- Farley, K. A., J. H. Natland, and H. Craig (1992), Binary mixing of enriched and undegassed (primitive-questionable) mantle components (He, Sr, Nd, Pb) in Samoan lavas, *Earth Planet. Sci. Lett.*, 111, 183–199.
- Georgen, J. E., M. D. Kurz, H. J. B. Dick, and J. Lin (2003), Low  $^3\text{He}/^4\text{He}$  ratios in basalt glasses from the western Southwest Indian Ridge (10°–24°E), *Earth Planet. Sci. Lett.*, 206, 509–528.
- Gonnermann, H. M., and S. Mukhopadhyay (2009), Preserving noble gases in a convecting mantle, *Nature*, 459, U560–U588.
- Graham, D. W. (2002), Noble gas isotope geochemistry of mid-ocean ridge and Ocean Island Basalts: Characterization of mantle source reservoirs, *Rev. Mineral. Geochem.*, 47, 247–317.
- Graham, D. W., W. J. Jenkins, J. G. Schilling, G. Thompson, M. D. Kurz, and S. E. Humphris (1992), Helium isotope geochemistry of midocean ridge basalts from the South-Atlantic, *Earth Planet. Sci. Lett.*, 110, 133–147.

- Harrison, D., P. Burnard, and G. Turner (1999), Noble gas behaviour and composition in the mantle: Constraints from the Iceland Plume, *Earth Planet. Sci. Lett.*, *171*, 199–207.
- Hart, S. R. (1984), A large-scale isotope anomaly in the southern-hemisphere mantle, *Nature*, *309*, 753–757.
- Hawkesworth, C. J., M. S. M. Mantovani, P. N. Taylor, and Z. Palacz (1986), Evidence from the Parana of South Brazil for a continental contribution to Dupal basalts, *Nature*, *322*, 356–359.
- Hebeda, E. H., L. Schultz, and M. Freundel (1987), Radiogenic, fissiogenic and nucleogenic noble gases in zircons, *Earth Planet. Sci. Lett.*, *85*(1–3), 79–90.
- Hilton, D. R., K. Gronvold, C. G. Macpherson, and P. R. Castillo (1999), Extreme He-3/He-4 ratios in northwest Iceland: Constraining the common component in mantle plumes, *Earth Planet. Sci. Lett.*, *173*, 53–60.
- Hilton, D. R., C. G. Macpherson, and T. R. Elliott (2000), Helium isotope ratios in mafic phenocrysts and geothermal fluids from La Palma, the Canary Islands (Spain): Implications for HIMU mantle sources, *Geochim. Cosmochim. Acta*, *64*, 2119–2132.
- Holland, G., and C. J. Ballentine (2006), Seawater subduction controls the heavy noble gas composition of the mantle, *Nature*, *441*, 186–191.
- Huang, S., C.-T. A. Lee, and Q.-Z. Yin (2014), Missing lead and high  $^3\text{He}/^4\text{He}$  in ancient sulfides associated with continental crust formation, *Sci. Rep.*, *4*, 5314.
- Hudson, G. B., B. M. Kennedy, F. A. Podosek, and C. M. Hohenberg (1989), The early Solar System abundance of Pu-244 as inferred from the St. Severin chondrite, in *Proceedings of 19th Lunar Planetary Science Conference*, pp. 547–557, Lunar and Planetary Institute, Houston, Texas.
- Iwamori, H., F. Albarede, and H. Nakamura (2010), Global structure of mantle isotopic heterogeneity and its implications for mantle differentiation and convection, *Earth Planet. Sci. Lett.*, *299*, 339–351.
- Jackson, M. G., and R. W. Carlson (2011), An ancient recipe for flood-basalt genesis, *Nature*, *476*, U316–U377.
- Jackson, M. G., and A. M. Jellinek (2013), Major and trace element composition of the high He-3/He-4 mantle: Implications for the composition of a nonchondritic Earth, *Geochim. Geophys. Geosyst.*, *14*, 2954–2976, doi:10.1002/ggge.20188.
- Jackson, M. G., R. W. Carlson, M. D. Kurz, P. D. Kempton, D. Francis, and J. Blusztajn (2010), Evidence for the survival of the oldest terrestrial mantle reservoir, *Nature*, *466*, U853–U884.
- Janney, P. E., A. P. Le Roex, and R. W. Carlson (2005), Hafnium isotope and trace element constraints on the nature of mantle heterogeneity beneath the central Southwest Indian Ridge (13 degrees E to 47 degrees E), *J. Petrol.*, *46*, 2427–2464.
- Kendrick, M. A., M. Scambelluri, M. Honda, and D. Phillips (2011), High abundances of noble gas and chlorine delivered to the mantle by serpentinite subduction, *Nat. Geosci.*, *4*, 807–812.
- Kunz, J., T. Staudacher, and C. J. Allegre (1998), Plutonium-fission xenon found in Earth's mantle, *Science*, *280*, 877–880.
- Kurz, M. D., and D. Geist (1999), Dynamics of the Galapagos hotspot from helium isotope geochemistry, *Geochim. Cosmochim. Acta*, *63*, 4139–4156.
- Kurz, M. D., W. J. Jenkins, and S. R. Hart (1982a), Helium isotopic systematics of oceanic islands and mantle heterogeneity, *Nature*, *297*, 43–47.
- Kurz, M. D., W. J. Jenkins, J. G. Schilling, and S. R. Hart (1982b), Helium isotopic variations in the mantle beneath the Central-North Atlantic-Ocean, *Earth Planet. Sci. Lett.*, *58*, 1–14.
- Kurz, M. D., W. J. Jenkins, S. R. Hart, and D. Clague (1983), Helium isotopic variations in volcanic rocks from Loihi seamount and the island of Hawaii, *Earth Planet. Sci. Lett.*, *66*, 388–406.
- Kurz, M. D., A. P. Le Roex, and H. J. B. Dick (1998), Isotope geochemistry of the oceanic mantle near the Bouvet triple junction, *Geochim. Cosmochim. Acta*, *62*, 841–852.
- Lee, C.-T. A., P. Luffi, T. Hoink, J. Li, R. Dasgupta, and J. Hernlund (2010), Upside-down differentiation and generation of a 'primordial' lower mantle, *Nature*, *463*, 930–933.
- Lewis, R. S. (1975), Rare-gases in separated whitlockite from St. Severin chondrite—Xenon and krypton from fission extinct Pu-244, *Geochim. Cosmochim. Acta*, *39*(4), 417–432.
- Mahoney, J., A. P. Leroex, Z. Peng, R. L. Fisher, and J. H. Natland (1992), Southwestern limits of Indian-Ocean ridge mantle and the origin of low  $^{206}\text{Pb}/^{204}\text{Pb}$  mid-ocean ridge basalt—Isotope systematics of the Central Southwest Indian Ridge (17°E–50°E), *J. Geophys. Res.*, *97*, 19,771–19,790.
- Moreira, M. (2013), Noble gas constraints on the origin and evolution of Earth's volatiles, *Geochim. Perspect.*, *2*, 229–403.
- Moreira, M., J. Kunz, and C. Allegre (1998), Rare gas systematics in Popping Rock: Isotopic and elemental compositions in the upper mantle, *Science*, *279*, 1178–1181.
- Moreira, M., R. Doucelance, M. D. Kurz, B. Dupre, and C. J. Allegre (1999), Helium and lead isotope geochemistry of the Azores Archipelago, *Earth Planet. Sci. Lett.*, *169*, 189–205.
- Mukhopadhyay, S. (2012), Early differentiation and volatile accretion recorded in deep-mantle neon and xenon, *Nature*, *486*, U101–U124.
- Ozima, M., F. A. Podosek, and G. Igarishi (1985), Terrestrial xenon isotope constraints on the early history of the Earth, *Nature*, *315*, 471–474.
- Parai, R., S. Mukhopadhyay, and J. C. Lassiter (2009), New constraints on the HIMU mantle from neon and helium isotopic compositions of basalts from the Cook-Austral Islands, *Earth Planet. Sci. Lett.*, *277*, 253–261.
- Parai, R., S. Mukhopadhyay, and J. J. Standish (2012), Heterogeneous upper mantle Ne, Ar and Xe isotopic compositions and a possible Dupal noble gas signature recorded in basalts from the Southwest Indian Ridge, *Earth Planet. Sci. Lett.*, *359*, 227–239.
- Parman, S. W., M. D. Kurz, S. R. Hart, and T. L. Grove (2005), Helium solubility in olivine and implications for high (3)He/(4)He in ocean island basalts, *Nature*, *437*, 1140–1143.
- Pepin, R. O. (1991), On the origin and early evolution of terrestrial planet atmospheres and meteoritic volatiles, *Icarus*, *92*(1), 2–79.
- Pepin, R. O. (2000), On the isotopic composition of primordial xenon in terrestrial planet atmospheres, *Space Sci. Rev.*, *92*(1–2), 371–395.
- Pepin, R. O., and D. Porcelli (2002), Origin of noble gases in the terrestrial planets, *Rev. Mineral. Geochem.*, *47*(1), 191–246.
- Pepin, R. O., and D. Porcelli (2006), Xenon isotope systematics, giant impacts, and mantle degassing on the early Earth, *Earth Planet. Sci. Lett.*, *250*, 470–485.
- Pepin, R. O., R. H. Becker, and P. E. Rider (1995), Xenon and krypton isotopes in extraterrestrial regolith soils and in the solar-wind, *Geochim. Cosmochim. Acta*, *59*(23), 4997–5022.
- Pető, M. K., S. Mukhopadhyay and K. A. Kelley (2013), Heterogeneities from the first 100 million years recorded in deep mantle noble gases from the Northern Lau Back-arc Basin, *Earth Planet. Sci. Lett.*, *369*, 13–23.
- Phinney, D., J. Tennyson, and U. Frick (1978), Xenon in CO<sub>2</sub> well gas revisited, *J. Geophys. Res.*, *83*, 2313–2319.
- Pujol, M., B. Marty, and R. Burgess (2011), Chondritic-like xenon trapped in Archean rocks: A possible signature of the ancient atmosphere, *Earth Planet. Sci. Lett.*, *308*, 298–306.

- Ragetli, R. A., E. H. Hebeda, P. Signer, and R. Wieler (1994), Uranium xenon chronology—Precise determination of  $\lambda(\text{SF})^* \text{Y136}(\text{SF})$  for spontaneous fission of U-238, *Earth Planet. Sci. Lett.*, *128*(3–4), 653–670.
- Standish, J. J. (2006), The influence of ridge geometry at the ultraslow-spreading Southwest Indian Ridge (9–25°E): Basalt composition sensitivity to variations in source and process, PhD thesis, Joint Prog. in Oceanogr./Appl. Ocean Sci. and Eng, Massachusetts Institute of Technology/Woods Hole Oceanographic Institute Joint Program in Oceanography, Woods Hole, Massachusetts.
- Standish, J. J., H. J. B. Dick, P. J. Michael, W. G. Melson and T. O'Hearn (2008), MORB generation beneath the ultraslow spreading Southwest Indian Ridge (9–25°E): Major element chemistry and the importance of process versus source, *Geochem. Geophys. Geosyst.*, *9*, Q05004, doi:10.1029/2008GC001959.
- Staudacher, T. (1987), Upper mantle origin for Harding County well gases, *Nature*, *325*, 605–607.
- Staudacher, T., and C. J. Allegre (1982), Terrestrial xenology, *Earth Planet. Sci. Lett.*, *60*, 389–406.
- Staudacher, T., and C. J. Allegre (1988), Recycling of oceanic-crust and sediments—The noble-gas subduction barrier, *Earth Planet. Sci. Lett.*, *89*, 173–183.
- Stuart, F. M., S. Lass-Evans, J. G. Fitton, and R. M. Ellam (2003), High  $^3\text{He}/^4\text{He}$  ratios in picritic basalts from Baffin Island and the role of a mixed reservoir in mantle plumes, *Nature*, *424*, 57–59.
- Trieloff, M., and J. Kunz (2005), Isotope systematics of noble gases in the Earth's mantle: Possible sources of primordial isotopes and implications for mantle structure, *Phys. Earth Planet. Inter.*, *148*, 13–38.
- Trieloff, M., J. Kunz, D. A. Clague, D. Harrison, and C. J. Allegre (2000), The nature of pristine noble gases in mantle plumes, *Science*, *288*, 1036–1038.
- Tucker, J. M., and S. Mukhopadhyay (2014), Evidence for multiple magma ocean outgassing and atmospheric loss episodes from mantle noble gases, *Earth Planet. Sci. Lett.*, *393*, 254–265.
- Tucker, J. M., S. Mukhopadhyay, and J. G. Schilling (2012), The heavy noble gas composition of the depleted MORB mantle (DMM) and its implications for the preservation of heterogeneities in the mantle, *Earth Planet. Sci. Lett.*, *355*, 244–254.
- Wetherill, G. W. (1953), Spontaneous fission yields from uranium and thorium, *Phys. Rev.*, *92*(4), 907–912.
- Wieler, R., and H. Baur (1994), Krypton and xenon from the solar-wind and solar energetic particles in 2 lunar ilmenites of different antiquity, *Meteoritics*, *29*(5), 570–580.
- York, D. (1969), Least squares fitting of a straight line with correlated errors, *Earth Planet. Sci. Lett.*, *5*, 320.
- York, D., N. M. Evensen, M. L. Martinez, J. D. Delgado (2004), Unified equations for the slope, intercept, and standard errors of the best straight line, *Am. J. Phys.*, *72*, 367–375.

4 **The evolution of MORB and plume mantle volatile budgets: constraints from**  
5 **fission Xe isotopes in Southwest Indian Ridge basalts**

6 Rita Parai<sup>a,†</sup>, Sujoy Mukhopadhyay<sup>b</sup>

7 <sup>a</sup>Department of Earth and Planetary Sciences, Harvard University, 20 Oxford Street, Cambridge, MA 02138,  
8 USA;

9 <sup>b</sup>Department of Earth and Planetary Sciences, University of California, Davis, 1 Shields Avenue, Davis, CA  
10 95616, USA

11 <sup>†</sup>Now at: Department of Terrestrial Magnetism, Carnegie Institution for Science, 5241 Broad Branch Road  
12 NW, Washington, DC 20015, USA

13  
14 **Contents of this file**

15  
16 **Text S1.** Linear Least Squares and Monte Carlo Error Propagation Methods

17 **Text S2.** A Note on Linear Least Squares Results for Well Gases

18 **Text S3.** Monte Carlo Linear Least Squares Results

19  
20 **Figure S1.** Reproducibility of  $^{129,130,131,134,136}\text{Xe}/^{132}\text{Xe}$  in air standards

21 **Figure S2.** Chi-square ( $\chi^2$ ) as a function of mantle endmember  $^{129}\text{Xe}/^{132}\text{Xe}$

22 **Figure S3.** Determinations of mantle source  $^{130,131,134,136}\text{Xe}/^{132}\text{Xe}$  for the SWIR  
23 Western Orthogonal Supersegment

24 **Figure S4.** Determinations of mantle source  $^{130,131,134,136}\text{Xe}/^{132}\text{Xe}$  for the SWIR  
25 Eastern Orthogonal Supersegment

26 **Figure S5.** Pie charts illustrating mixing proportions of  $^{132}\text{Xe}$  in mantle sources  
27 given solar wind initial mantle Xe composition

28 **Figure S6.** Pie charts illustrating mixing proportions of  $^{132}\text{Xe}$  in mantle sources  
29 given U-Xe initial mantle Xe composition  
30

31 **Introduction**

32 This supplementary material contains detailed descriptions of our numerical methods, a  
33 full set of Monte Carlo model outputs, 6 supplementary figures and supplementary  
34 references. The Southwest Indian Ridge basalt Xe isotopic data were collected during 4  
35 analytical sessions spanning two years. The first supplementary figure illustrates our  
36 instrument stability during the analysis period. The next three figures illustrate the  
37 methods used to find the best fit mantle source Xe isotopic compositions corrected for  
38 syn- to post-eruptive atmospheric contamination. The last two figures show results of the  
39 linear least squares minimization to solve for the mixing proportions of  $^{132}\text{Xe}$  from an  
40 initial mantle Xe budget (solar wind or U-Xe), atmospheric recycling, Pu-fission and U-  
41 fission.

42 **Text S1. Linear Least Squares and Monte Carlo Error Propagation Methods**

43 We used the built-in Matlab function *lsqlin* to solve our constrained linear  
44 least squares problem. Mantle source  $^{130}\text{Xe}/^{132}\text{Xe}$ ,  $^{131}\text{Xe}/^{132}\text{Xe}$ ,  $^{134}\text{Xe}/^{132}\text{Xe}$  and  
45  $^{136}\text{Xe}/^{132}\text{Xe}$  isotopic compositions can each be described using equations of the  
46 form:

47

$$x_{init} \left( \frac{\zeta \text{Xe}}{^{132}\text{Xe}} \right)_{init} + x_{atm} \left( \frac{\zeta \text{Xe}}{^{132}\text{Xe}} \right)_{atm} + x_{Pu} \left( \frac{\zeta \text{Xe}}{^{132}\text{Xe}} \right)_{Pu} + x_U \left( \frac{\zeta \text{Xe}}{^{132}\text{Xe}} \right)_U = \left( \frac{\zeta \text{Xe}}{^{132}\text{Xe}} \right)_{mantle} \quad \text{Eq. S1}$$

48 where  $\zeta = ^{130}\text{Xe}$ ,  $^{131}\text{Xe}$ ,  $^{134}\text{Xe}$  and  $^{136}\text{Xe}$ ;  $x$  is the molar mixing proportion of  $^{132}\text{Xe}$ ;  
49 *init* designates the initial mantle composition, modeled here using either solar  
50 wind, average carbonaceous chondrite (AVCC) or U-Xe; *atm* designates recycled  
51 atmospheric Xe; *Pu* designates Pu-fission Xe; and *U* designates U-fission Xe.  
52 The Xe isotope ratios of the components are given in Table 3. This gives us four  
53 linear equations with four unknowns. We can treat this as a linear algebra  
54 problem, where we wish to find the least squares solution to the linear expression  
55  $\mathbf{Ax} = \mathbf{b}$ , where:

56

57

58

59 A is a matrix of mixing endmember isotopic compositions (Table 3):

$$A = \begin{pmatrix} \left[ \begin{array}{c} {}^{130}\text{Xe} \\ {}^{132}\text{Xe} \end{array} \right]_{init} & \left[ \begin{array}{c} {}^{130}\text{Xe} \\ {}^{132}\text{Xe} \end{array} \right]_{atm} & \left[ \begin{array}{c} {}^{130}\text{Xe} \\ {}^{132}\text{Xe} \end{array} \right]_{Pu} & \left[ \begin{array}{c} {}^{130}\text{Xe} \\ {}^{132}\text{Xe} \end{array} \right]_U \\ \left[ \begin{array}{c} {}^{131}\text{Xe} \\ {}^{132}\text{Xe} \end{array} \right]_{init} & \left[ \begin{array}{c} {}^{131}\text{Xe} \\ {}^{132}\text{Xe} \end{array} \right]_{atm} & \left[ \begin{array}{c} {}^{131}\text{Xe} \\ {}^{132}\text{Xe} \end{array} \right]_{Pu} & \left[ \begin{array}{c} {}^{131}\text{Xe} \\ {}^{132}\text{Xe} \end{array} \right]_U \\ \left[ \begin{array}{c} {}^{134}\text{Xe} \\ {}^{132}\text{Xe} \end{array} \right]_{init} & \left[ \begin{array}{c} {}^{134}\text{Xe} \\ {}^{132}\text{Xe} \end{array} \right]_{atm} & \left[ \begin{array}{c} {}^{134}\text{Xe} \\ {}^{132}\text{Xe} \end{array} \right]_{Pu} & \left[ \begin{array}{c} {}^{134}\text{Xe} \\ {}^{132}\text{Xe} \end{array} \right]_U \\ \left[ \begin{array}{c} {}^{136}\text{Xe} \\ {}^{132}\text{Xe} \end{array} \right]_{init} & \left[ \begin{array}{c} {}^{136}\text{Xe} \\ {}^{132}\text{Xe} \end{array} \right]_{atm} & \left[ \begin{array}{c} {}^{136}\text{Xe} \\ {}^{132}\text{Xe} \end{array} \right]_{Pu} & \left[ \begin{array}{c} {}^{136}\text{Xe} \\ {}^{132}\text{Xe} \end{array} \right]_U \end{pmatrix} \quad \text{Eq. S2}$$

60

61  $\mathbf{x}$  is a vector of unknown mixing proportions of  ${}^{132}\text{Xe}$ :

$$\mathbf{x} = \begin{pmatrix} x_{init} \\ x_{atm} \\ x_{Pu} \\ x_U \end{pmatrix} \quad \text{Eq. S3}$$

62 And  $\mathbf{b}$  is a vector of mantle source Xe isotopic compositions:

$$\mathbf{b} = \begin{pmatrix} \left[ \begin{array}{c} {}^{130}\text{Xe} \\ {}^{132}\text{Xe} \end{array} \right]_{mantle} \\ \left[ \begin{array}{c} {}^{131}\text{Xe} \\ {}^{132}\text{Xe} \end{array} \right]_{mantle} \\ \left[ \begin{array}{c} {}^{134}\text{Xe} \\ {}^{132}\text{Xe} \end{array} \right]_{mantle} \\ \left[ \begin{array}{c} {}^{136}\text{Xe} \\ {}^{132}\text{Xe} \end{array} \right]_{mantle} \end{pmatrix} \quad \text{Eq. S4}$$

63 The problem is subject to a further constraint in that the  ${}^{132}\text{Xe}$  mixing proportions

64 must sum to 1:

$$x_{init} + x_{atm} + x_{Pu} + x_U = 1 \quad \text{Eq. S5}$$

65 and each mixing proportion must fall between 0 and 1:

66  $0 \leq x \leq 1$  for each component.

67 Matlab's *lsqlin* function solves linear least squares problems subject to  
68 optionally specified additional constraints. In our case, we have an equality  
69 constraint corresponding to Eq. S5:

$$70 \quad \mathbf{F}\mathbf{x} = \mathbf{g}, \text{ where } \mathbf{F} = \begin{pmatrix} 1 \\ 1 \\ 1 \\ 1 \end{pmatrix} \text{ and } \mathbf{g} = 1 \quad \text{Eq. S6}$$

71 and lower and upper bounds on  $\mathbf{x}$ :

$$72 \quad \mathbf{lb} = \begin{pmatrix} 0 \\ 0 \\ 0 \\ 0 \end{pmatrix} \quad \text{Eq. S7}$$

$$73 \quad \mathbf{ub} = \begin{pmatrix} 1 \\ 1 \\ 1 \\ 1 \end{pmatrix} \quad \text{Eq. S8}$$

74 For numerical stability, the lower bounds are set to  $10^{-5}$  rather than 0 (Eq. S7).

75 The full Matlab command used to solve the mixing problem is therefore:

```
76 [x resnorm resd eflag]=lsqlin(comp_norm,mantle_norm,[],[],F,g,lb,ub)
```

77 We note that we normalize the mixing component compositions  
78 (*comp\_norm*) and the mantle isotopic compositions (*mantle\_norm*) to the  $1\sigma$   
79 standard deviations on the mantle isotopic compositions, such that the residuals  
80 are computed in units of  $\sigma$  and the minimized sum of squared residuals  
81 corresponds to minimizing chi-square.  $\mathbf{x}$  is the solution vector, *resnorm* is the sum  
82 of squared residuals, *resd* is a vector of the residuals for each isotope ratio equal  
83 to  $\mathbf{Ax} - \mathbf{b}$ , and *eflag* is an exit flag that serves as an indication that the  
84 optimization was successful.

85 We use a Monte Carlo method to propagate the uncertainties in the  
86 mantle source isotopic compositions through to determine the uncertainties in the

87 mixing proportions. This is accomplished by repeatedly sampling mantle  
88 compositions (for the vector  $\mathbf{b}$ , Eq. S4) from within the  $1\sigma$  error space around the  
89 mantle source composition (using normal distributions based on the values and  
90 uncertainties in Table 4), computing the normalized  $\text{mantle\_norm}$  and then solving  
91 for  $\mathbf{x}$ . We then compute  $^{129}\text{Xe}^*/^{136}\text{Xe}$  and  $^{136}\text{Xe}_{\text{Pu}}/(^{136}\text{Xe}_{\text{Pu}}+^{136}\text{Xe}_{\text{U}})$  using the  
92 equations given in the main text (Eqs. 3-7). We exclude model realizations where  
93 the absolute value of any individual residual exceeds 2 (i.e., any element of  $\text{resd}$   
94 is greater than 2 or less than -2), which indicates that the best fit solution is more  
95 than  $2\sigma$  away from the mantle source Xe composition in at least one Xe isotope  
96 ratio. After screening for the quality of the fit, we collect statistics on the  
97 distributions of the individual mixing proportions in  $\mathbf{x}$  after  $10^6$  realizations and  
98 compute medians, 68% and 95% confidence intervals.

99 Below we give full result tables and histograms exploring the results for  
100 MORB sources (SWIR Western Orthogonal Supersegment and SWIR Eastern  
101 Orthogonal Supersegment from this study; Equatorial Atlantic depleted mantle  
102 from Tucker et al., 2012; and well gas from Holland and Ballentine, 2006 and  
103 Caffee et al., 1999) and plume-influenced sources (Iceland from Mukhopadhyay,  
104 2012; and the Rochambeau Rift from Petó et al., 2013).

## 105 **Text S2. A Note on Linear Least Squares Results for Well Gases**

106 Continental well gases sample noble gases derived from the upper  
107 mantle, but they are affected by contributions from both crustal U-fission and  
108 shallow atmospheric contamination. We cannot correct for these two  
109 contaminants to determine the well gas mantle source Xe composition as we did

110 with the basalt data, and so we must use measured well gas Xe compositions  
111 instead. We perform our linear least squares determinations using the Harding  
112 County, NM data from Caffee et al. (1999) and the error-weighted average of the  
113 two most mantle-like data from Bravo Dome, NM (Holland and Ballentine, 2006).  
114 We emphasize that well gas mixing proportion results are not directly comparable  
115 to results from basalts: we obtain mixing proportions for the initial mantle Xe, the  
116 *total* atmospheric Xe contribution (both recycled and shallow-level  
117 contamination), Pu-fission Xe and *total* U-fission Xe (from both the mantle source  
118 and the continental crust that hosts the well gas). Based on these computations,  
119 we are able to estimate the mantle source  $^{129}\text{Xe}^*/^{136}\text{Xe}_{\text{Pu}}$ . Below we show the full  
120 model output results for well gases, but we note that the  $^{136}\text{Xe}_{\text{Pu}}/(^{136}\text{Xe}_{\text{Pu}} + ^{136}\text{Xe}_{\text{U}})$   
121 ratio given here is a lower limit for the mantle source  $^{136}\text{Xe}_{\text{Pu}}/(^{136}\text{Xe}_{\text{Pu}} + ^{136}\text{Xe}_{\text{U}})$ ,  
122 since a crustal U-fission contribution lowers the ratio. We further note that a large  
123 U-fission contribution sometimes makes it difficult to resolve the Pu-fission  
124 component for well gases from zero given the precision in the data. A poorly-  
125 resolved Pu fission proportion generates a spuriously high  $^{129}\text{Xe}^*/^{136}\text{Xe}_{\text{Pu}}$  ratio  
126 (see results for Harding County and Bravo dome well gases using U-Xe as the  
127 initial mantle). Therefore, we do not include the U-Xe well gas results in our  
128 computation of the MORB group average  $^{129}\text{Xe}^*/^{136}\text{Xe}_{\text{Pu}}$ .

### 129 **Text S3. Monte Carlo Linear Least Squares Results**

130 For each sample location, we give a table of quantile statistics describing  
131 the distributions of results (the median, 68% confidence limits, and the 95%  
132 confidence limits) for the mixing fractions of  $^{132}\text{Xe}$  from initial mantle, recycled

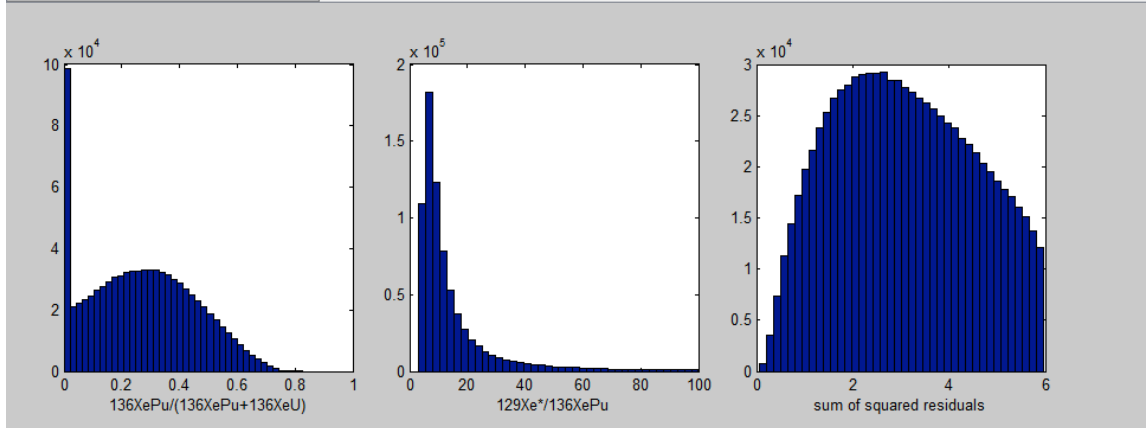
133 atmosphere, U-fission Xe and Pu-fission Xe; as well as the  $^{129}\text{Xe}^*/^{136}\text{Xe}_{\text{Pu}}$  and  
 134  $^{136}\text{Xe}_{\text{Pu}}/(^{136}\text{Xe}_{\text{Pu}} + ^{136}\text{Xe}_{\text{U}})$  ratios. We also show histograms for the  $^{129}\text{Xe}^*/^{136}\text{Xe}_{\text{Pu}}$   
 135 and  $^{136}\text{Xe}_{\text{Pu}}/(^{136}\text{Xe}_{\text{Pu}} + ^{136}\text{Xe}_{\text{U}})$  ratios and for the sum of squared residuals for  
 136  $^{130}\text{Xe}/^{132}\text{Xe}$ ,  $^{131}\text{Xe}/^{132}\text{Xe}$ ,  $^{134}\text{Xe}/^{132}\text{Xe}$  and  $^{136}\text{Xe}/^{132}\text{Xe}$ . We note that a model  
 137 realization that fits all four mantle source isotope ratios within  $1\sigma$  has a sum of  
 138 squared residuals below 4. Least squares solutions obtained using ~3.5 Ga chert  
 139 Xe (Pujol et al., 2011) as the recycled atmospheric Xe composition frequently  
 140 had sum of squared residuals in excess of ~50, indicating that the best solutions  
 141 using ancient air compositions were still very poor fits of the mantle composition.

142 **Mid-ocean ridge basalts**

143 **SWIR Western Orthogonal Supersegment**

**SWIR Western Orthogonal Supersegment with initial mantle =AVCC**

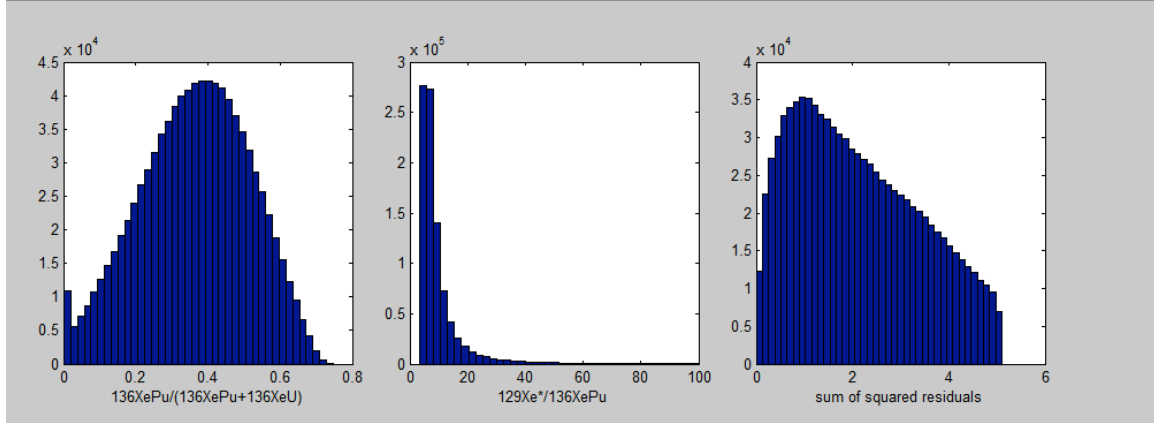
	95% conf lower limit	68% conf lower limit	median	68% conf upper limit	95% conf upper limit
initial mantle	0.009	0.047	0.110	0.179	0.235
recycled atm	0.717	0.776	0.850	0.919	0.958
Pu-fission	0.000	0.003	0.014	0.026	0.035
U-fission	0.014	0.019	0.025	0.032	0.033
$^{129}\text{Xe}^*/^{136}\text{Xe}_{\text{Pu}}$	4.4	6.0	10.8	51.1	1558.5
$^{136}\text{Xe}_{\text{Pu}}/(^{136}\text{Xe}_{\text{Pu}} + ^{136}\text{Xe}_{\text{U}})$	0.00	0.06	0.27	0.47	0.62



144

**SWIR Western Orthogonal Supersegment with initial mantle =solar\_wind**

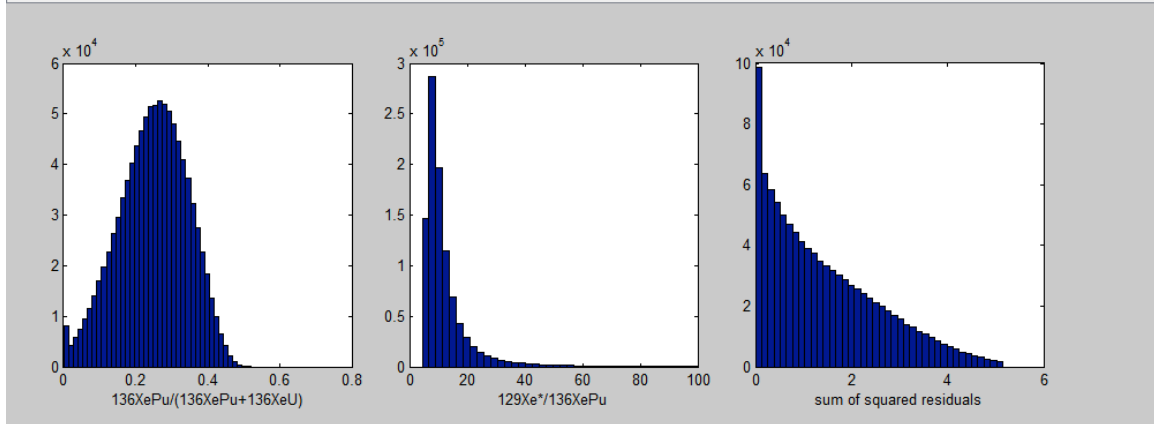
	95% conf lower limit	68% conf lower limit	median	68% conf upper limit	95% conf upper limit
initial mantle	0.046	0.094	0.155	0.216	0.263
recycled atm	0.682	0.733	0.800	0.866	0.918
Pu-fission	0.003	0.011	0.022	0.032	0.041
U-fission	0.015	0.019	0.024	0.029	0.033
$^{129}\text{Xe}^*/^{136}\text{XePu}$	4.0	5.0	7.3	13.9	51.3
$^{136}\text{XePu}/(^{136}\text{XePu}+^{136}\text{XeU})$	0.06	0.20	0.37	0.52	0.63



145  
146  
147

**SWIR Western Orthogonal Supersegment with initial mantle =U-Xe**

	95% conf lower limit	68% conf lower limit	median	68% conf upper limit	95% conf upper limit
initial mantle	0.077	0.126	0.186	0.246	0.295
recycled atm	0.649	0.702	0.767	0.832	0.885
Pu-fission	0.003	0.009	0.016	0.023	0.029
U-fission	0.026	0.028	0.031	0.033	0.035
$^{129}\text{Xe}^*/^{136}\text{XePu}$	5.5	6.9	9.8	17.5	51.5
$^{136}\text{XePu}/(^{136}\text{XePu}+^{136}\text{XeU})$	0.05	0.15	0.25	0.35	0.42



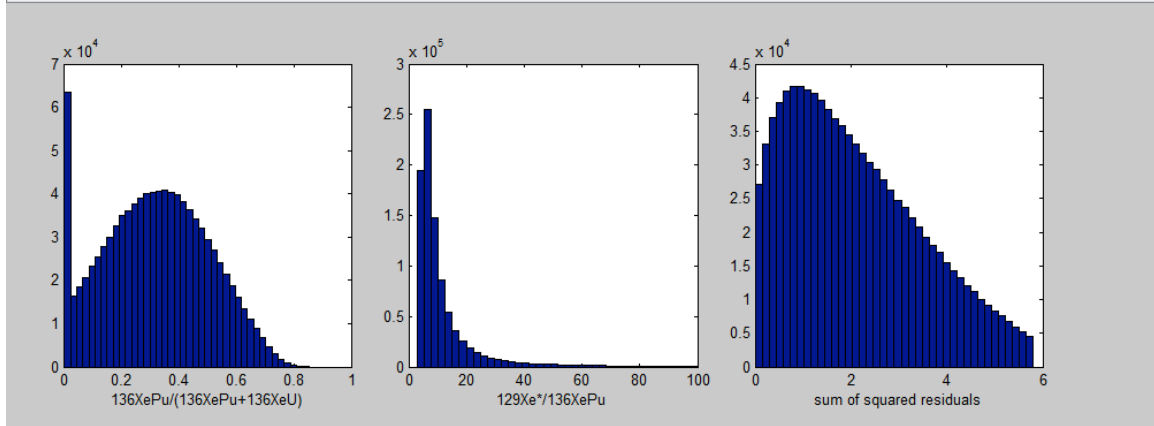
148  
149  
150  
151

152  
153  
154

**SWIR Eastern Orthogonal Supersegment**

**SWIR Eastern Orthogonal Supersegment with initial mantle =AVCC**

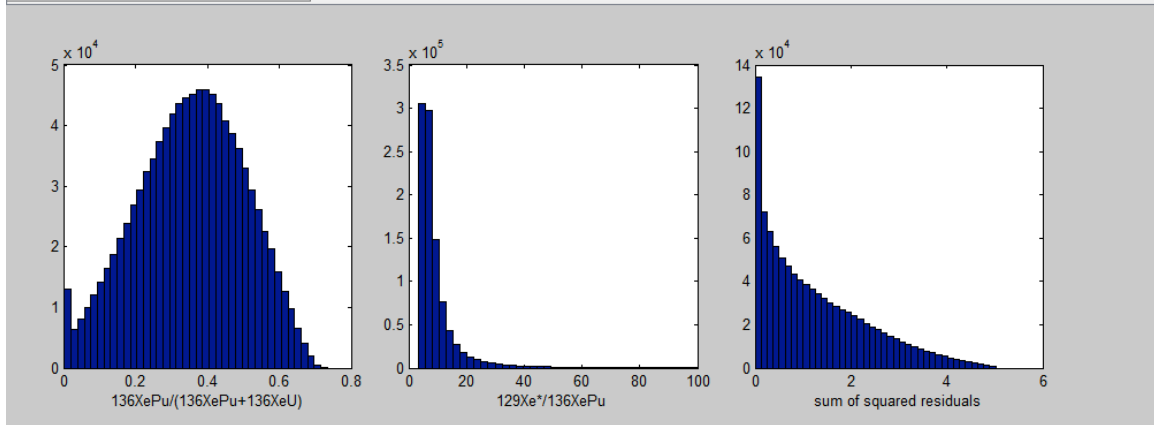
	95% conf lower limit	68% conf lower limit	median	68% conf upper limit	95% conf upper limit
initial mantle	0.017	0.044	0.083	0.124	0.157
recycled atm	0.813	0.849	0.892	0.935	0.962
Pu-fission	0.000	0.004	0.011	0.017	0.023
U-fission	0.007	0.010	0.014	0.018	0.020
$^{129}\text{Xe}^*/^{136}\text{XePu}$	3.8	5.1	8.3	22.9	877.3
$^{136}\text{XePu}/(^{136}\text{XePu}+^{136}\text{XeU})$	0.00	0.12	0.32	0.51	0.67



155  
156

**SWIR Eastern Orthogonal Supersegment with initial mantle =solar\_wind**

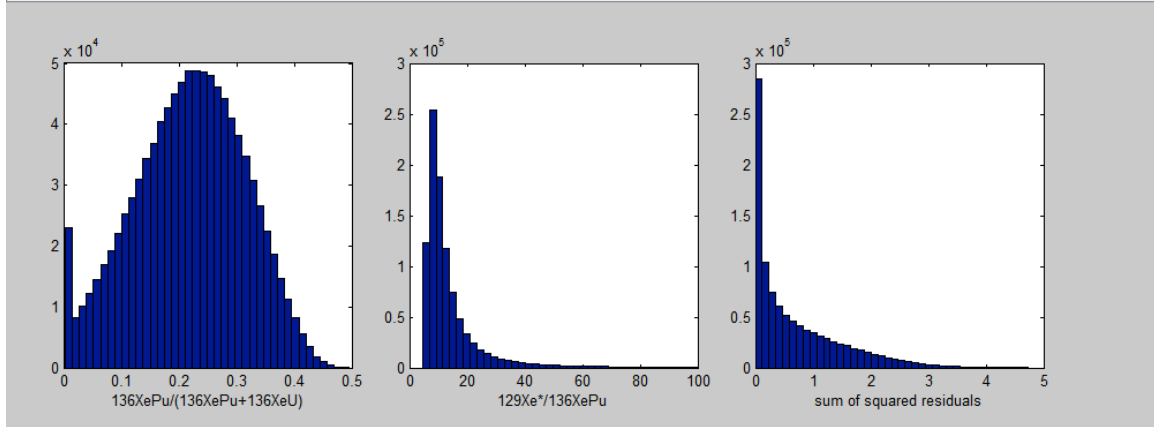
	95% conf lower limit	68% conf lower limit	median	68% conf upper limit	95% conf upper limit
initial mantle	0.032	0.060	0.096	0.132	0.160
recycled atm	0.807	0.837	0.876	0.916	0.946
Pu-fission	0.002	0.007	0.013	0.019	0.024
U-fission	0.009	0.012	0.015	0.017	0.020
$^{129}\text{Xe}^*/^{136}\text{XePu}$	3.9	4.9	7.1	13.5	52.1
$^{136}\text{XePu}/(^{136}\text{XePu}+^{136}\text{XeU})$	0.05	0.20	0.36	0.51	0.62



157  
158

**SWIR Eastern Orthogonal Supersegment with initial mantle =U-Xe**

	95% conf lower limit	68% conf lower limit	median	68% conf upper limit	95% conf upper limit
initial mantle	0.043	0.072	0.107	0.143	0.173
recycled atm	0.795	0.826	0.865	0.903	0.934
Pu-fission	0.001	0.004	0.009	0.013	0.016
U-fission	0.016	0.017	0.019	0.021	0.022
$^{129}\text{Xe}^*/^{136}\text{XePu}$	5.6	7.2	10.6	21.3	141.9
$^{136}\text{XePu}/(^{136}\text{XePu}+^{136}\text{XeU})$	0.02	0.12	0.22	0.32	0.39

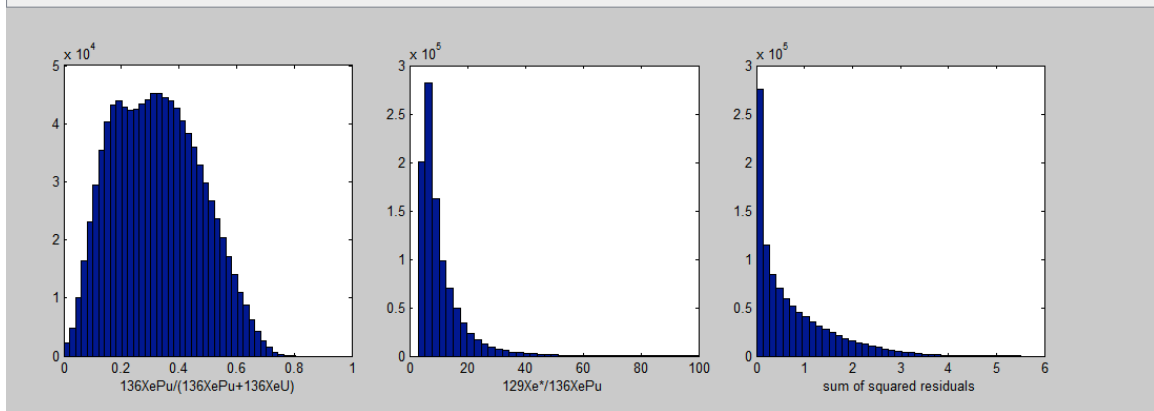


159  
160  
161  
162  
163  
164  
165

**Equatorial Atlantic depleted MORB (Tucker et al., 2012)**

**Equatorial Atlantic Depleted MORB (Tucker et al., 2012) with initial mantle =AVCC**

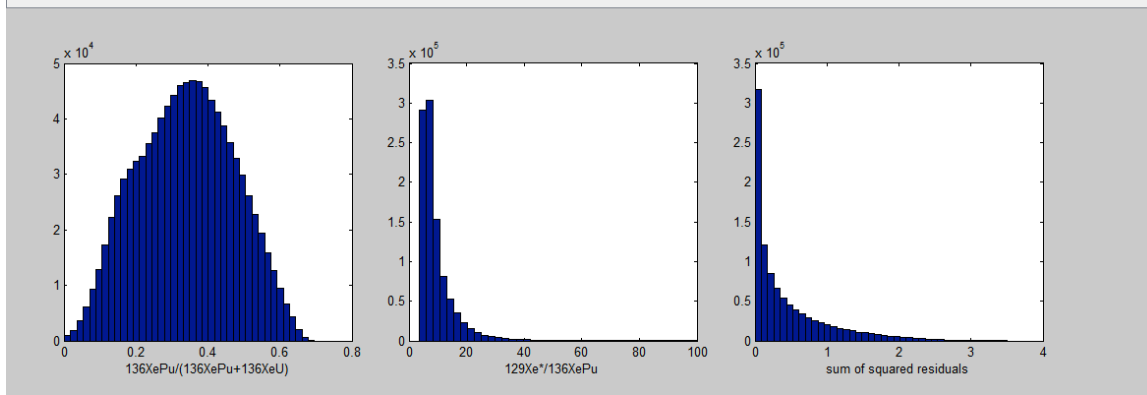
	95% conf lower limit	68% conf lower limit	median	68% conf upper limit	95% conf upper limit
initial mantle	0.000	0.007	0.071	0.136	0.187
recycled atm	0.759	0.814	0.883	0.952	0.961
Pu-fission	0.004	0.010	0.019	0.030	0.039
U-fission	0.015	0.020	0.026	0.032	0.035
$^{129}\text{Xe}^*/^{136}\text{XePu}$	4.0	5.1	8.1	16.3	36.0
$^{136}\text{XePu}/(^{136}\text{XePu}+^{136}\text{XeU})$	0.07	0.16	0.32	0.49	0.62



166  
167

**Equatorial Atlantic Depleted MORB (Tucker et al., 2012) with initial mantle =solar\_wind**

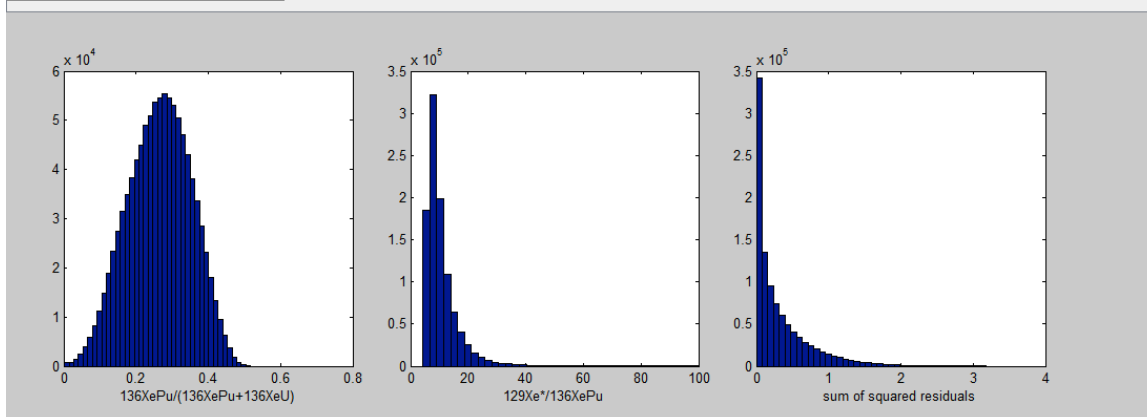
	95% conf lower limit	68% conf lower limit	median	68% conf upper limit	95% conf upper limit
initial mantle	0.000	0.026	0.084	0.143	0.189
recycled atm	0.753	0.804	0.868	0.932	0.960
Pu-fission	0.005	0.012	0.022	0.032	0.040
U-fission	0.018	0.022	0.027	0.031	0.034
$^{129}\text{Xe}/^{136}\text{XePu}$	4.0	5.0	7.3	13.6	28.1
$^{136}\text{XePu}/(^{136}\text{XePu}+^{136}\text{XeU})$	0.09	0.19	0.34	0.48	0.59



168  
169

**Equatorial Atlantic Depleted MORB (Tucker et al., 2012) with initial mantle =U-Xe**

	95% conf lower limit	68% conf lower limit	median	68% conf upper limit	95% conf upper limit
initial mantle	0.000	0.034	0.091	0.149	0.197
recycled atm	0.747	0.799	0.861	0.923	0.959
Pu-fission	0.006	0.011	0.017	0.024	0.030
U-fission	0.026	0.028	0.031	0.033	0.035
$^{129}\text{Xe}/^{136}\text{XePu}$	5.3	6.5	9.0	14.7	27.5
$^{136}\text{XePu}/(^{136}\text{XePu}+^{136}\text{XeU})$	0.09	0.17	0.27	0.36	0.42



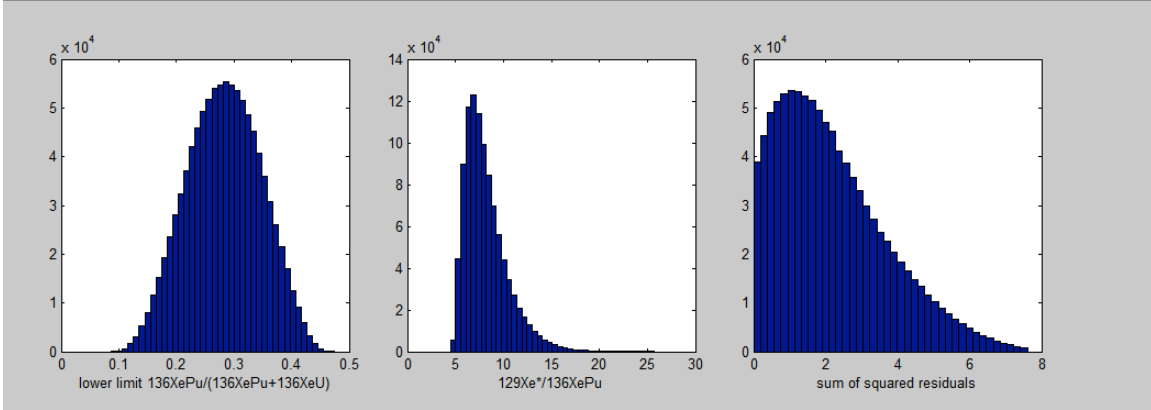
170  
171  
172  
173

174

**Harding County well gas (Caffee et al., 1999)**

**Harding Co. Well Gas (Caffee et al., 1999) with initial mantle =AVCC**

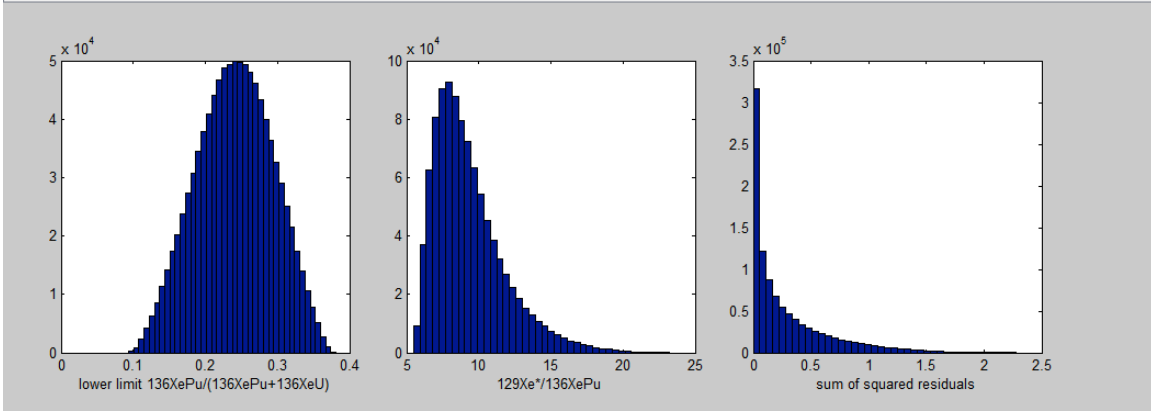
	95% conf lower limit	68% conf lower limit	median	68% conf upper limit	95% conf upper limit
initial mantle	0.090	0.103	0.119	0.135	0.148
recycled + shallow atm	0.821	0.835	0.852	0.869	0.883
Pu-fission	0.006	0.008	0.011	0.014	0.016
U-fission from mantle + crust	0.015	0.016	0.018	0.019	0.021
$^{129}\text{Xe}*/^{136}\text{XePu}$	5.3	6.2	7.7	10.2	13.9
LOWER LIMIT $^{136}\text{XePu}/(^{136}\text{XePu}+^{136}\text{XeU})$	0.16	0.22	0.28	0.35	0.40



175  
176

**Harding Co. Well Gas (Caffee et al., 1999) with initial mantle =solar\_wind**

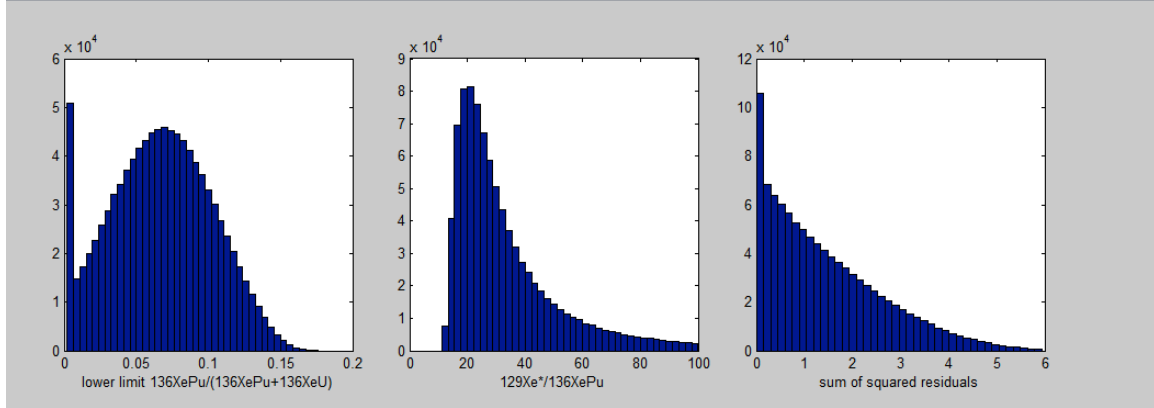
	95% conf lower limit	68% conf lower limit	median	68% conf upper limit	95% conf upper limit
initial mantle	0.089	0.101	0.115	0.130	0.142
recycled + shallow atm	0.825	0.838	0.854	0.870	0.883
Pu-fission	0.006	0.008	0.010	0.013	0.015
U-fission from mantle + crust	0.018	0.019	0.020	0.022	0.023
$^{129}\text{Xe}*/^{136}\text{XePu}$	6.1	7.1	8.8	11.6	15.7
LOWER LIMIT $^{136}\text{XePu}/(^{136}\text{XePu}+^{136}\text{XeU})$	0.14	0.19	0.24	0.30	0.34



177  
178

**Harding Co. Well Gas (Caffee et al., 1999) with initial mantle =U-Xe**

	95% conf lower limit	68% conf lower limit	median	68% conf upper limit	95% conf upper limit
initial mantle	0.087	0.099	0.114	0.129	0.141
recycled + shallow atm	0.827	0.841	0.857	0.873	0.885
Pu-fission	0.000	0.001	0.003	0.005	0.006
U-fission from mantle + crust	0.025	0.026	0.026	0.027	0.028
$^{129}\text{Xe}^*/^{136}\text{XePu}$	14.5	18.9	29.6	68.9	876.8
LOWER LIMIT $^{136}\text{XePu}/(^{136}\text{XePu}+^{136}\text{XeU})$	0.00	0.03	0.07	0.10	0.13

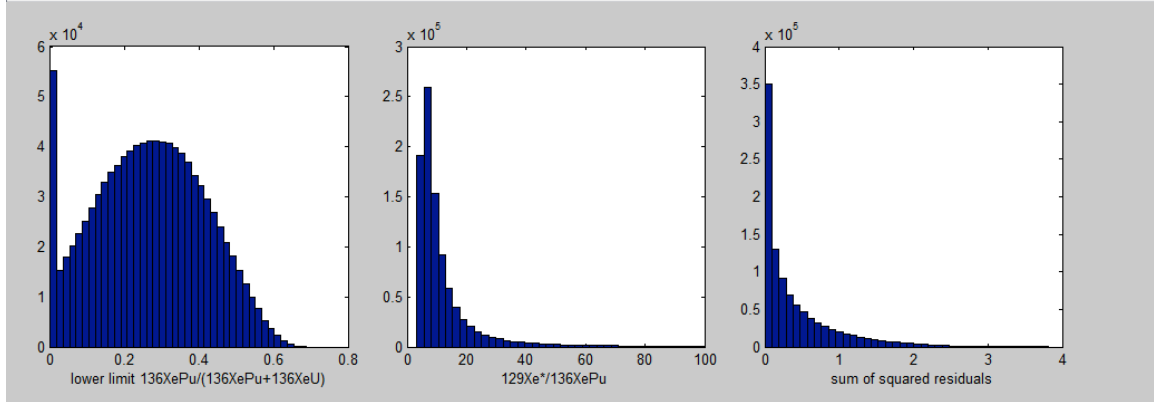


179  
180  
181  
182  
183  
184  
185

**Bravo Dome Well Gas (Holland and Ballentine, 2006)**

**Bravo Dome Well Gas (Holland and Ballentine, 2006) with initial mantle =AVCC**

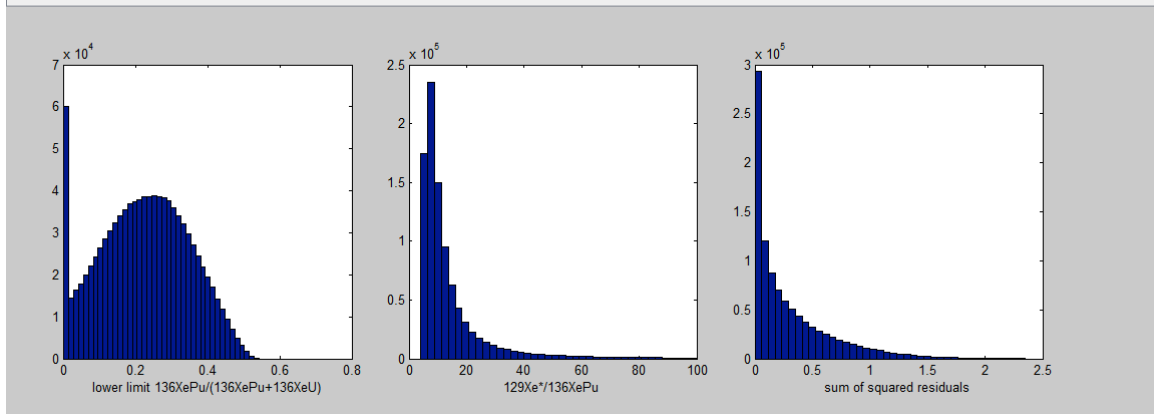
	95% conf lower limit	68% conf lower limit	median	68% conf upper limit	95% conf upper limit
initial mantle	0.033	0.058	0.095	0.132	0.161
recycled + shallow atm	0.806	0.838	0.878	0.917	0.943
Pu-fission	0.000	0.004	0.010	0.016	0.021
U-fission from mantle + crust	0.011	0.014	0.017	0.021	0.023
$^{129}\text{Xe}^*/^{136}\text{XePu}$	4.2	5.4	8.8	22.8	882.3
LOWER LIMIT $^{136}\text{XePu}/(^{136}\text{XePu}+^{136}\text{XeU})$	0.00	0.11	0.27	0.43	0.54



186  
187

**Bravo Dome Well Gas (Holland and Ballentine, 2006) with initial mantle =solar\_wind**

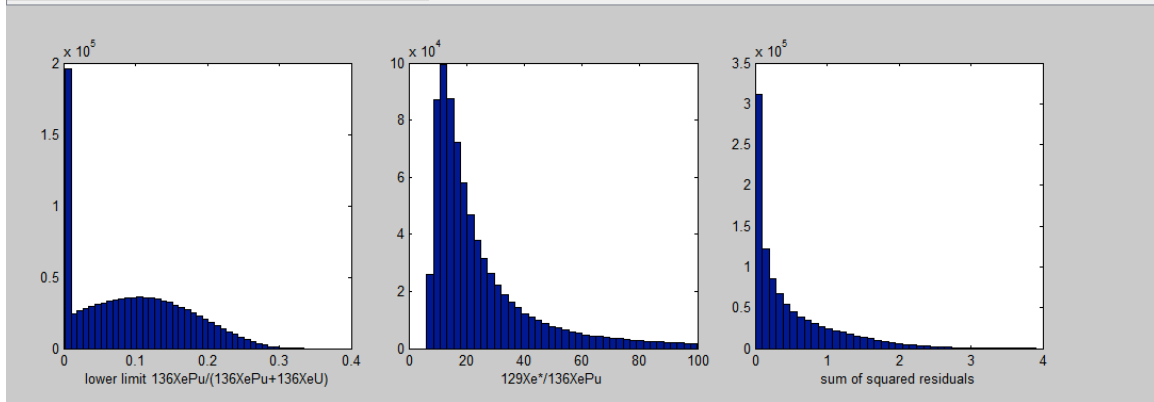
	95% conf lower limit	68% conf lower limit	median	68% conf upper limit	95% conf upper limit
initial mantle	0.032	0.053	0.086	0.119	0.144
recycled + shallow atm	0.822	0.850	0.886	0.921	0.945
Pu-fission	0.000	0.003	0.009	0.015	0.019
U-fission from mantle + crust	0.015	0.017	0.020	0.022	0.024
$^{129}\text{Xe}^*/^{136}\text{XePu}$	4.9	6.3	10.2	27.0	897.7
LOWER LIMIT $^{136}\text{XePu}/(^{136}\text{XePu}+^{136}\text{XeU})$	0.00	0.09	0.23	0.36	0.45



188  
189

**Bravo Dome Well Gas (Holland and Ballentine, 2006) with initial mantle =U-Xe**

	95% conf lower limit	68% conf lower limit	median	68% conf upper limit	95% conf upper limit
initial mantle	0.035	0.055	0.082	0.114	0.140
recycled + shallow atm	0.827	0.855	0.890	0.920	0.940
Pu-fission	0.000	0.000	0.004	0.008	0.011
U-fission from crust + mantle	0.021	0.022	0.024	0.025	0.026
$^{129}\text{Xe}^*/^{136}\text{XePu}$	8.5	11.9	24.0	896.5	903.1
LOWER LIMIT $^{136}\text{XePu}/(^{136}\text{XePu}+^{136}\text{XeU})$	0.00	0.00	0.09	0.18	0.24



190  
191  
192

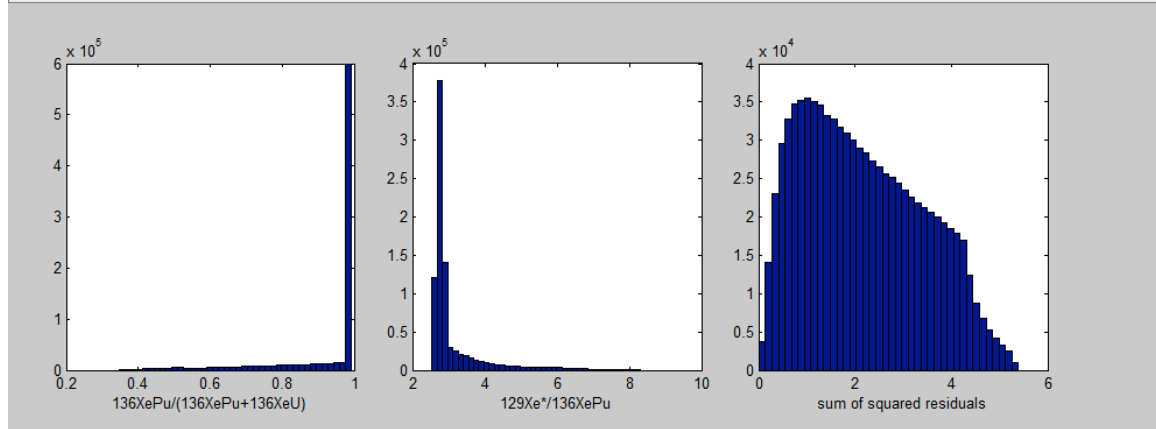
193  
 194  
 195  
 196  
 197  
 198

**Plume-influenced basalts**

**DICE – Iceland (Mukhopadhyay, 2012)**

**DICE - Iceland (Mukhopadhyay, 2012) with initial mantle =AVCC**

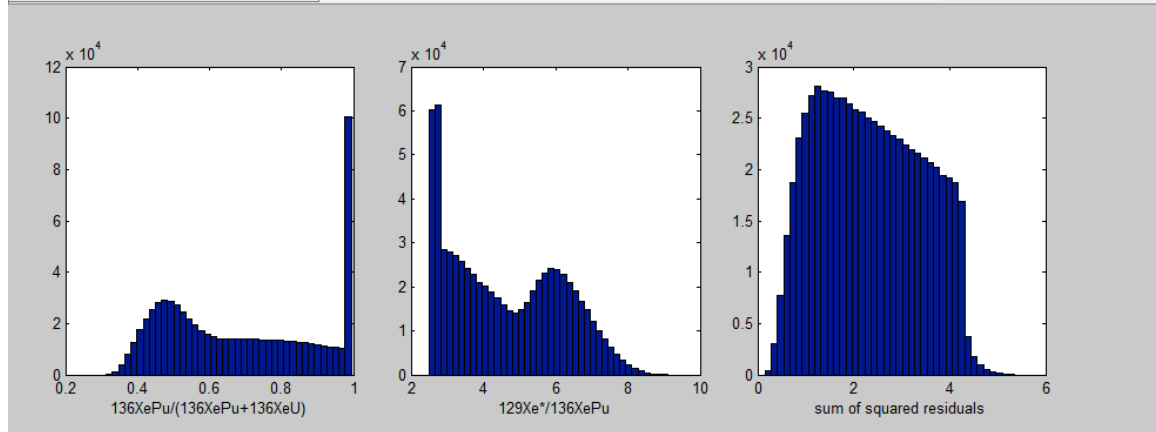
	95% conf lower limit	68% conf lower limit	median	68% conf upper limit	95% conf upper limit
initial mantle	0.002	0.042	0.065	0.076	0.085
recycled atm	0.893	0.903	0.915	0.939	0.983
Pu-fission	0.010	0.016	0.020	0.021	0.022
U-fission	0.000	0.000	0.000	0.003	0.006
$^{129}\text{Xe}^*/^{136}\text{XePu}$	2.6	2.7	2.8	3.5	6.0
$^{136}\text{XePu}/(^{136}\text{XePu}+^{136}\text{XeU})$	0.49	0.80	0.99	0.99	0.99



199  
 200

**DICE - Iceland (Mukhopadhyay, 2012) with initial mantle =solar\_wind**

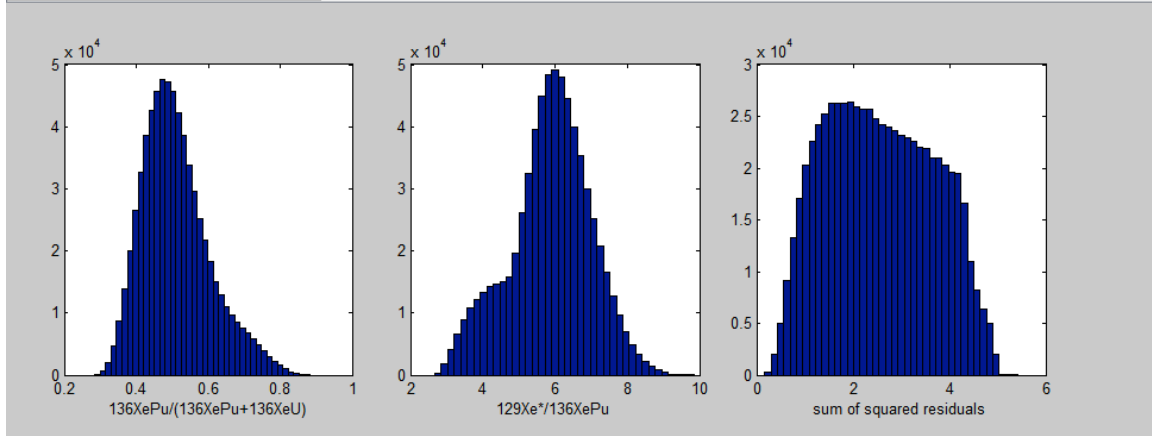
	95% conf lower limit	68% conf lower limit	median	68% conf upper limit	95% conf upper limit
initial mantle	0.000	0.000	0.023	0.065	0.081
recycled atm	0.896	0.913	0.959	0.984	0.985
Pu-fission	0.008	0.009	0.013	0.022	0.023
U-fission	0.000	0.001	0.005	0.007	0.008
$^{129}\text{Xe}^*/^{136}\text{XePu}$	2.6	2.8	4.4	6.4	7.5
$^{136}\text{XePu}/(^{136}\text{XePu}+^{136}\text{XeU})$	0.39	0.46	0.65	0.96	0.99



201  
 202

**DICE - Iceland (Mukhopadhyay, 2012) with initial mantle =U-Xe**

	95% conf lower limit	68% conf lower limit	median	68% conf upper limit	95% conf upper limit
initial mantle	0.000	0.000	0.000	0.023	0.058
recycled atm	0.921	0.959	0.984	0.985	0.985
Pu-fission	0.007	0.008	0.010	0.012	0.017
U-fission	0.004	0.005	0.006	0.007	0.008
$^{129}\text{Xe}^*/^{136}\text{XePu}$	3.5	4.7	5.9	7.0	8.0
$^{136}\text{XePu}/(^{136}\text{XePu}+^{136}\text{XeU})$	0.36	0.42	0.50	0.60	0.73

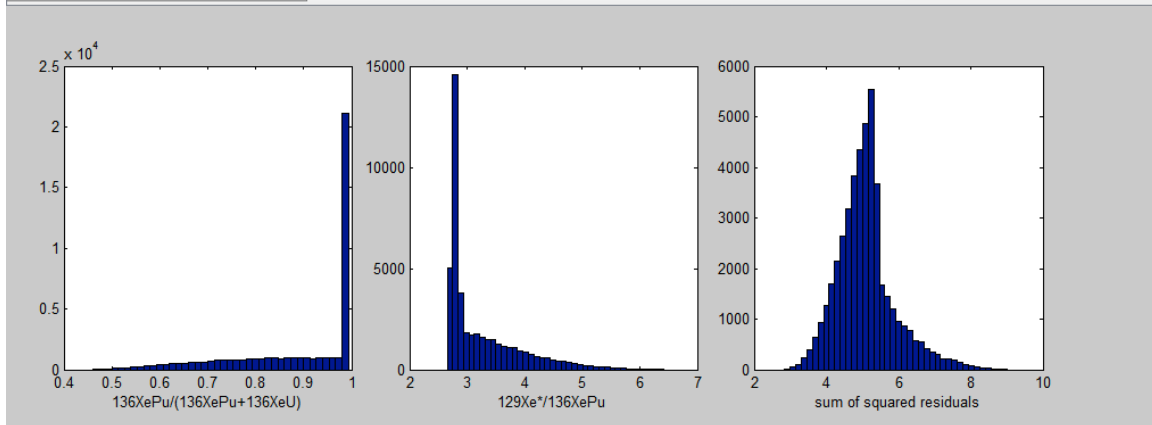


203  
204  
205  
206  
207

**NLD27 – Rochambeau Rift (Petó et al., 2013)**

**NLD27 - Rochambeau Rift (Peto et al., 2013) with initial mantle =AVCC**

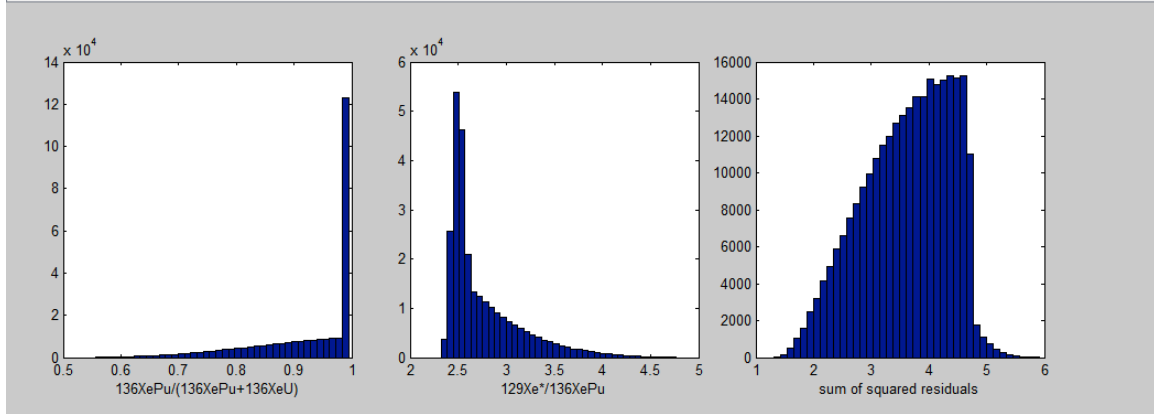
	95% conf lower limit	68% conf lower limit	median	68% conf upper limit	95% conf upper limit
initial mantle	0.064	0.083	0.110	0.121	0.128
recycled atm	0.850	0.858	0.869	0.898	0.919
Pu-fission	0.012	0.015	0.021	0.022	0.022
U-fission	0.000	0.000	0.001	0.004	0.006
$^{129}\text{Xe}^*/^{136}\text{XePu}$	2.7	2.8	2.9	3.9	5.1
$^{136}\text{XePu}/(^{136}\text{XePu}+^{136}\text{XeU})$	0.57	0.73	0.95	0.99	0.99



208  
209

**NLD27 - Rochambeau Rift (Peto et al., 2013) with initial mantle =solar\_wind**

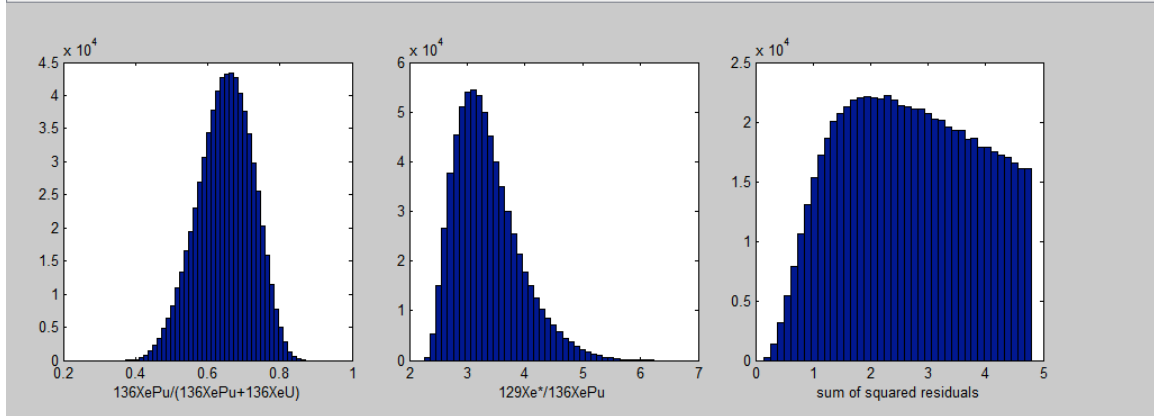
	95% conf lower limit	68% conf lower limit	median	68% conf upper limit	95% conf upper limit
initial mantle	0.091	0.113	0.136	0.152	0.165
recycled atm	0.808	0.822	0.839	0.864	0.888
Pu-fission	0.016	0.020	0.025	0.026	0.027
U-fission	0.000	0.000	0.001	0.003	0.005
$^{129}\text{Xe}*/^{136}\text{XePu}$	2.4	2.5	2.6	3.1	3.8
$^{136}\text{XePu}/(^{136}\text{XePu}+^{136}\text{XeU})$	0.69	0.82	0.97	0.99	0.99



210  
211

**NLD27 - Rochambeau Rift (Peto et al., 2013) with initial mantle =U-Xe**

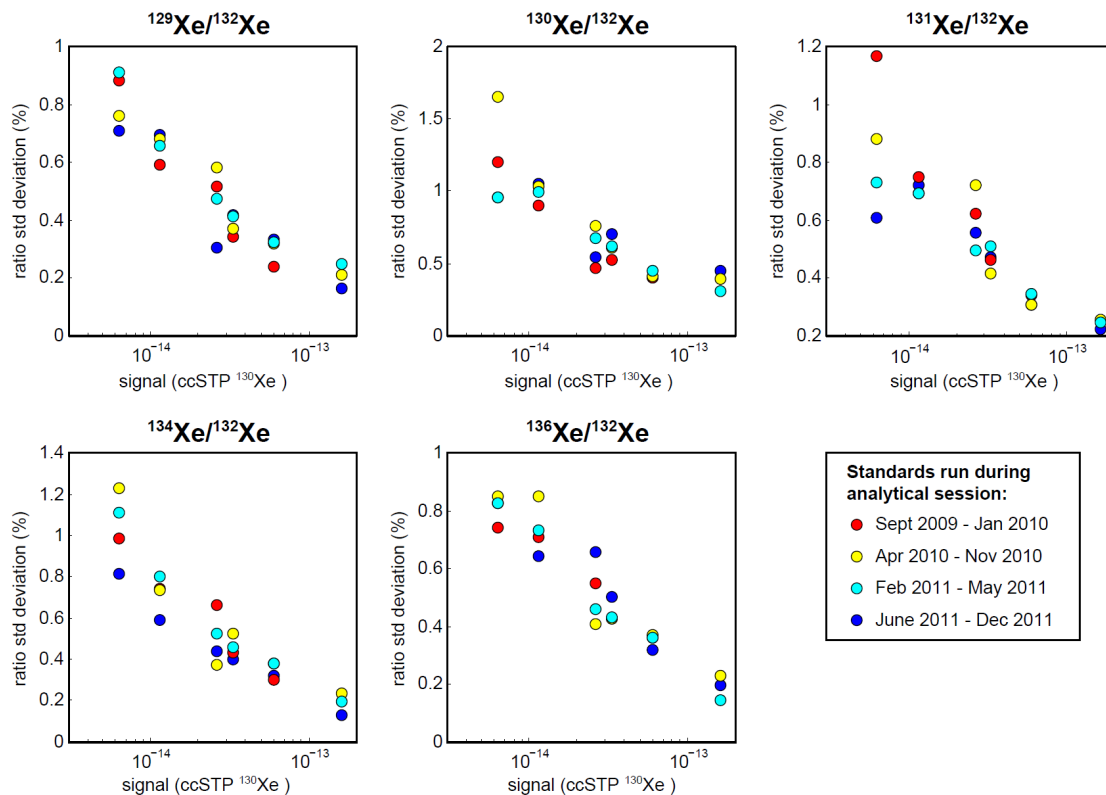
	95% conf lower limit	68% conf lower limit	median	68% conf upper limit	95% conf upper limit
initial mantle	0.112	0.135	0.163	0.189	0.211
recycled atm	0.759	0.782	0.811	0.841	0.866
Pu-fission	0.013	0.016	0.020	0.023	0.026
U-fission	0.004	0.006	0.007	0.008	0.009
$^{129}\text{Xe}*/^{136}\text{XePu}$	2.5	2.8	3.3	3.9	4.7
$^{136}\text{XePu}/(^{136}\text{XePu}+^{136}\text{XeU})$	0.49	0.57	0.65	0.72	0.78



212  
213  
214

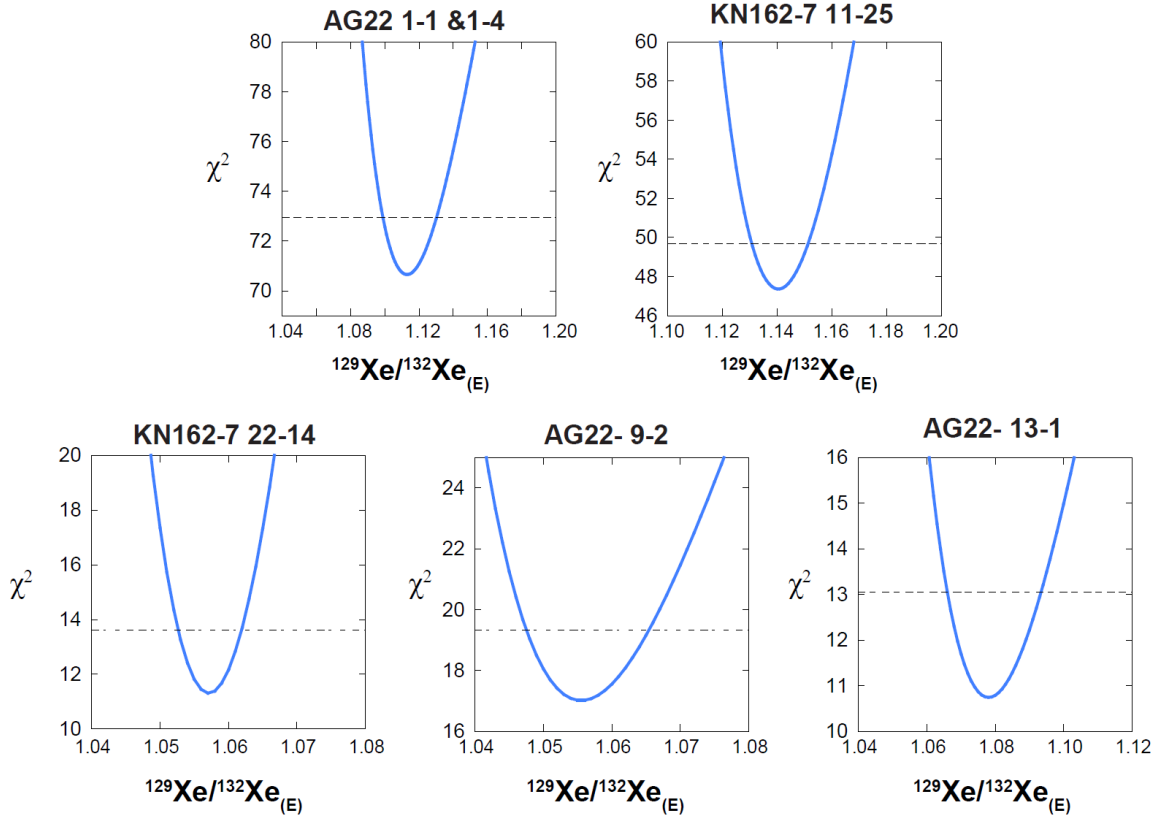
215

216  
217



218  
219

220 **Figure S1:** Reproducibility of  $^{129,130,131,134,136}\text{Xe}/^{132}\text{Xe}$  in Air standards over four different  
 221 analytical sessions. The percent standard deviation in the specified Xe isotope ratio is  
 222 shown as a function of signal size in units of cubic centimeters of  $^{130}\text{Xe}$  at standard  
 223 temperature and pressure. Instrument performance was found to be stable over four  
 224 different analytical sessions conducted over the span of two years.  
 225



226

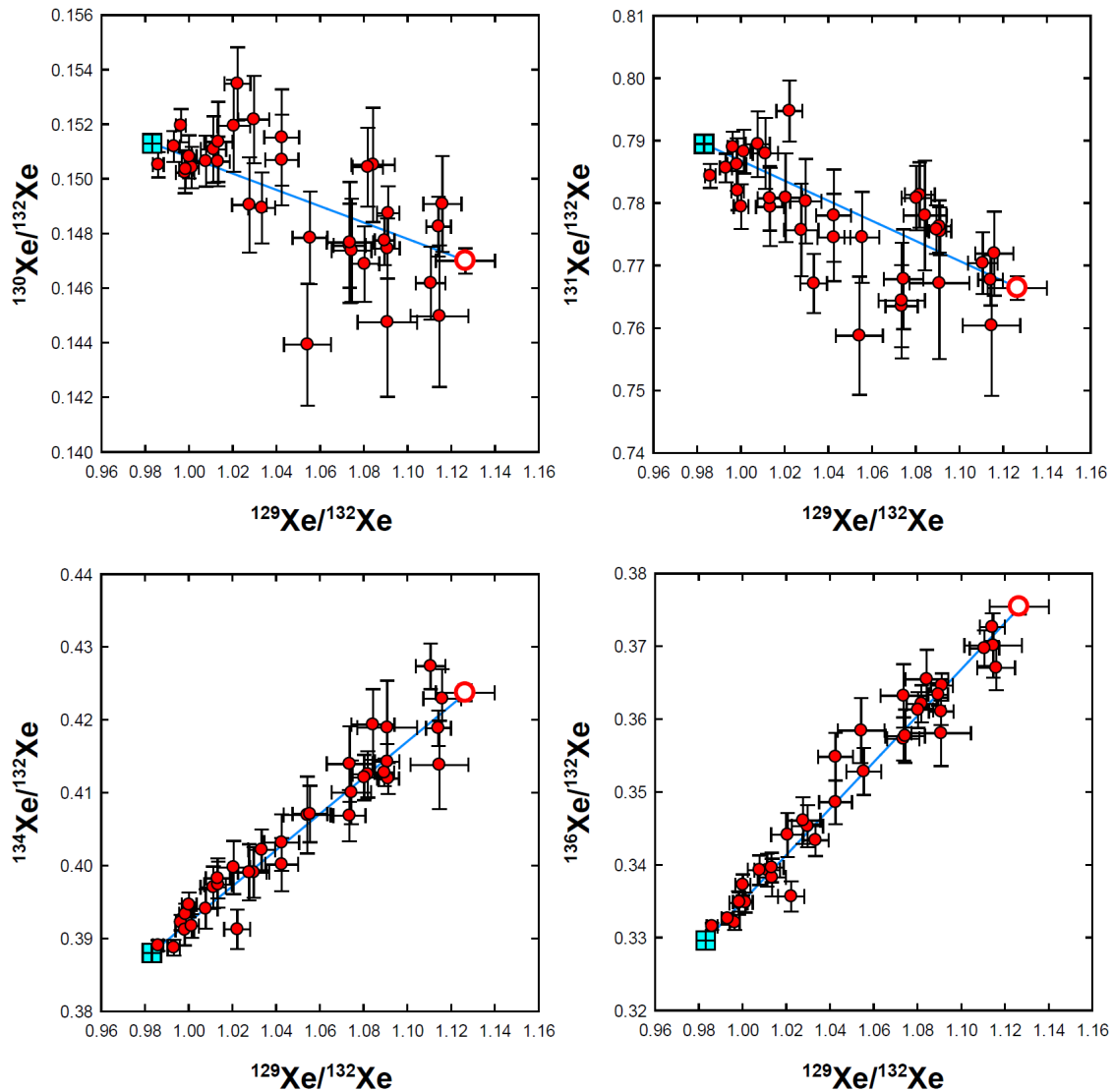
227 **Figure S2:** Chi-square ( $\chi^2$ ) as a function of mantle endmember  $^{129}\text{Xe}/^{132}\text{Xe}$  given free  
 228 variation in curvature for SWIR Orthogonal Supersegment samples. Air contamination  
 229 generates hyperbolic trends in  $^{129}\text{Xe}/^{132}\text{Xe} - ^{40}\text{Ar}/^{36}\text{Ar}$  space. The curvature of a two-  
 230 component mixing hyperbolic array is parameterized as  $\mathbf{k} =$   
 231  $(^{132}\text{Xe}/^{36}\text{Ar})_{\text{mantle}} / (^{132}\text{Xe}/^{36}\text{Ar})_{\text{atm}}$ . We use a grid search to find the combination of  $\mathbf{k}$  and  
 232 mantle source  $^{129}\text{Xe}/^{132}\text{Xe}$  (corresponding to mantle source  $^{40}\text{Ar}/^{36}\text{Ar}$  determined  
 233 previously; Parai et al., 2012) that minimizes the  $\chi^2$  cost function:

$$234 \quad \chi^2 = \sum_{i=1}^N \left[ \left( \frac{x_i - m_i}{\sigma_{xi}} \right)^2 + \left( \frac{y_i - n_i}{\sigma_{yi}} \right)^2 \right] \quad (\text{Eq. S9})$$

235 where  $(x_i \pm \sigma_{xi}, y_i \pm \sigma_{yi})$  are the  $N$  observed data points for a given sample and  $(m_i, n_i)$  are  
 236 the  $\sigma$ -normalized closest points to the data along a candidate hyperbola (i.e., the points  
 237 that minimize  $\chi^2$  for the candidate hyperbola). Since there are two free parameters in the

238 hyperbolic fit ( $k$  and mantle  $^{129}\text{Xe}/^{132}\text{Xe}$ ), the 68.3% confidence interval on the mantle  
 239  $^{129}\text{Xe}/^{132}\text{Xe}$  is defined where  $\chi^2 \leq \chi^2_{\min} + 2.30$  (Press et al., 1992).  
 240

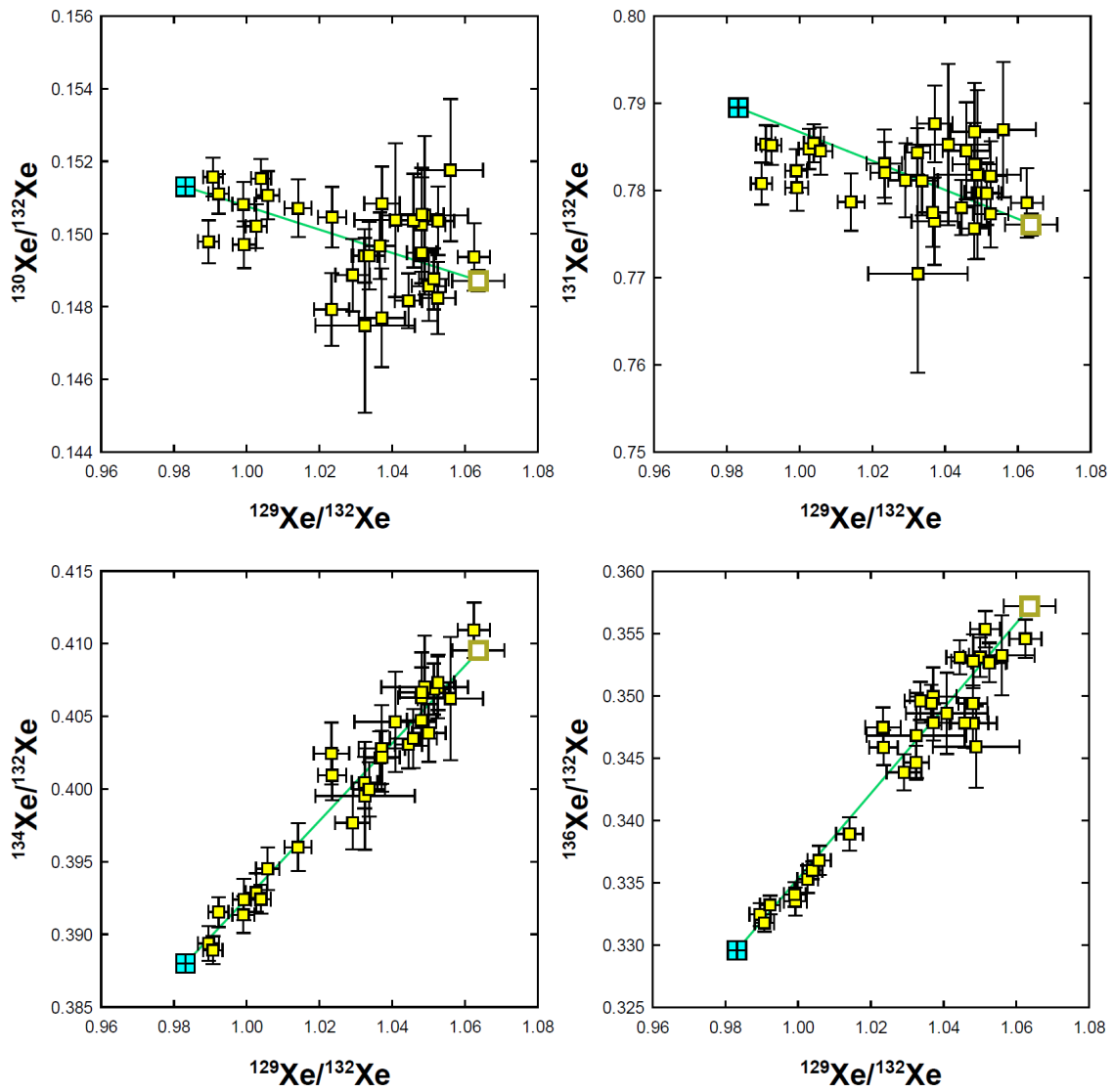
### SWIR Western Orthogonal Supersegment



241  
 242 **Figure S3:** Least squares determinations of mantle source  $^{130,131,134,136}\text{Xe}/^{132}\text{Xe}$  ratios  
 243 (bold open symbols) for the SWIR Western Orthogonal Supersegment.

244

## SWIR Eastern Orthogonal Supersegment



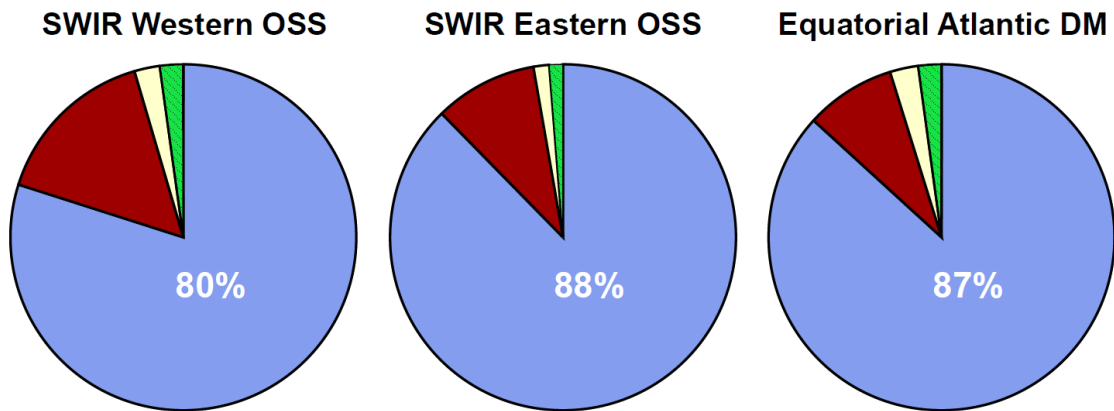
245

246 **Figure S4:** Least squares determinations of mantle source  $^{130,131,134,136}\text{Xe}/^{132}\text{Xe}$  ratios

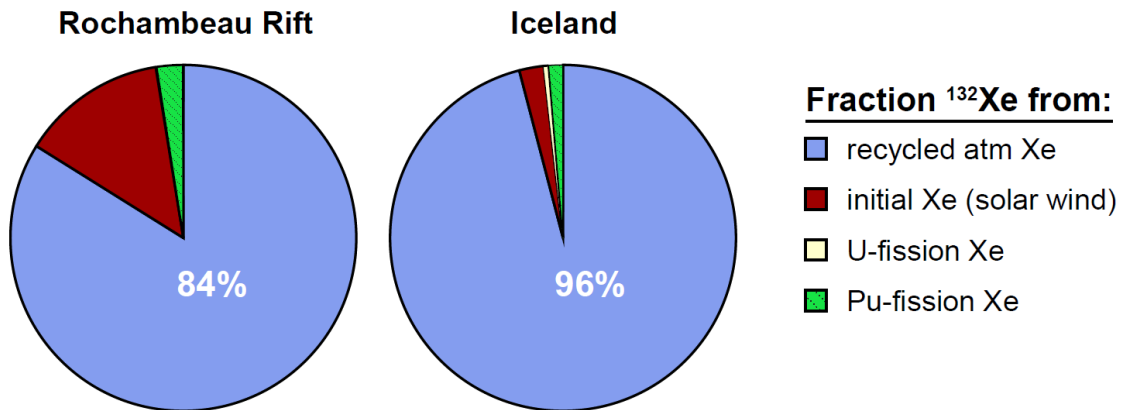
247 (bold open symbols) for the SWIR Eastern Orthogonal Supersegment.

248

**Mid-ocean ridge basalts:**



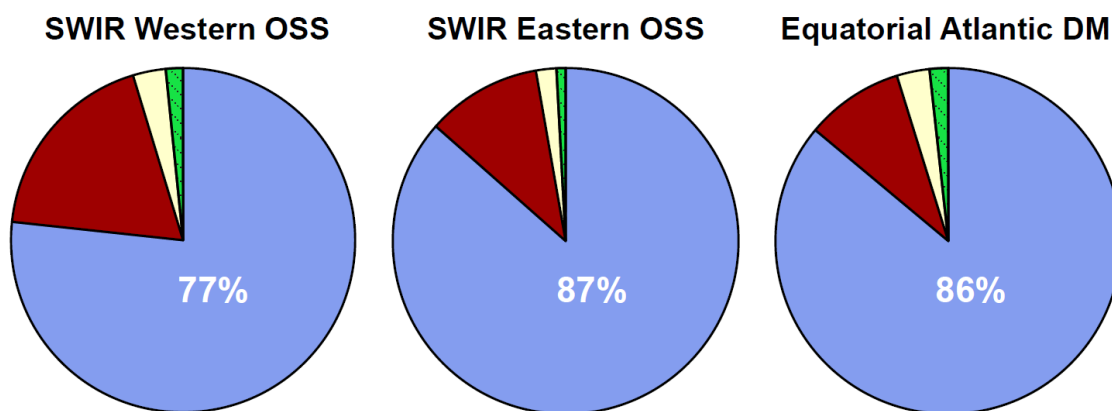
**Plume-influenced basalts:**



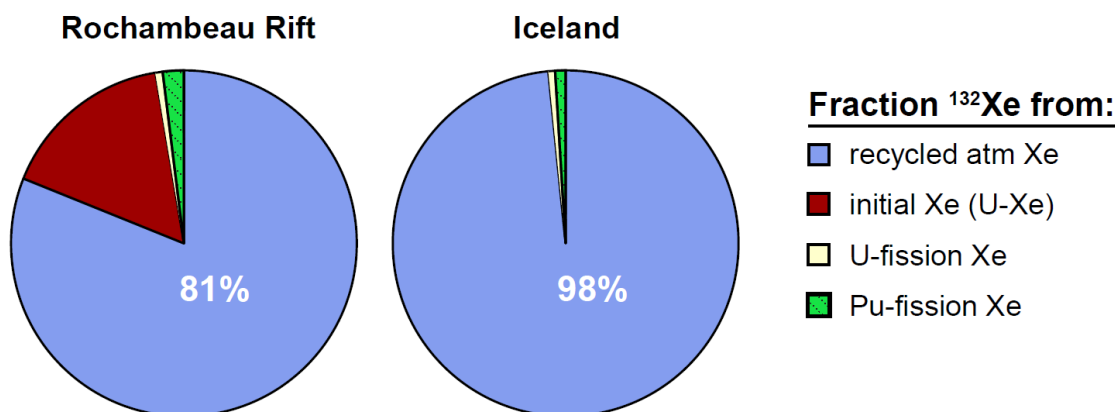
249

250 **Figure S5:** Pie charts illustrating the median proportions of present-day mantle  $^{132}\text{Xe}$   
251 derived from recycled atmosphere, initial mantle (solar wind), U-fission and Pu-fission in  
252 SWIR Western and Eastern Orthogonal Supersegment mantle sources. Results for  
253 Equatorial Atlantic depleted MORB (Tucker et al., 2012), Rochambeau Rift (Petó et al.,  
254 2013) and Iceland (Mukhopadhyay, 2012) are shown for comparison. Recycled  
255 atmospheric Xe uniformly dominates the mantle Xe budget (percentages given in white).  
256 Fission Xe in the mantle sources of plume-influenced basalts is primarily derived from  
257 Pu-fission.

**Mid-ocean ridge basalts:**



**Plume-influenced basalts:**



258

259

260 **Figure S6:** Pie charts illustrating the median proportions of present-day mantle  $^{132}\text{Xe}$   
261 derived from recycled atmosphere, initial mantle (U-Xe), U-fission and Pu-fission in  
262 SWIR Western and Eastern Orthogonal Supersegment mantle sources. Results for  
263 Equatorial Atlantic depleted MORB (Tucker et al., 2012), Rochambeau Rift (Petó et al.,  
264 2013) and Iceland (Mukhopadhyay, 2012) are shown for comparison. Recycled  
265 atmospheric Xe uniformly dominates the mantle Xe budget (percentages given in white).

266

267 **References**

- 268 Caffee, M.W., G. B. Hudson, C. Velsko, G. R. Huss, E. C. Alexander Jr., and A. R.  
269 Chivas (1999). Primordial noble gases from Earth's mantle: Identification of a  
270 primitive volatile component. *Science*, 285(5436): 2115-2118.
- 271 Holland, G. and C. J. Ballentine (2006). Seawater subduction controls the heavy noble  
272 gas composition of the mantle. *Nature*, 441(7090): 186-191.
- 273 Mukhopadhyay, S., 2012. Early differentiation and volatile accretion recorded in deep-  
274 mantle neon and xenon. *Nature* 486, 101-104, doi: 10.1038/Nature11141.
- 275 Parai, R., S. Mukhopadhyay, and J.J. Standish (2012). Heterogeneous upper mantle Ne,  
276 Ar and Xe isotopic compositions and a possible Dupal noble gas signature  
277 recorded in basalts from the Southwest Indian Ridge. *Earth and Planetary  
278 Science Letters*, 359: 227-239.
- 279 Pető, M.K., S. Mukhopadhyay, and K.A. Kelley (2013). Heterogeneities from the first 100  
280 million years recorded in deep mantle noble gases from the Northern Lau Back-  
281 arc Basin. *Earth and Planetary Science Letters*, 369: 13-23.
- 282 Pujol, M., B. Marty, R. Burgess (2011). Chondritic-like xenon trapped in Archean rocks:  
283 A possible signature of the ancient atmosphere. *Earth Planet. Sci. Lett.*, 308:  
284 298-306.
- 285 Press, W.H., S.A. Teukolsky, W.T. Vetterling, B.P. Flannery (1992). *Numerical Recipes*  
286 *in C: The Art of Scientific Computing*, second edition, Cambridge University  
287 Press, New York.
- 288 Tucker, J. M., S. Mukhopadhyay, J.G. Schilling (2012). The heavy noble gas  
289 composition of the depleted MORB mantle (DMM) and its implications for the  
290 origin of heterogeneities in the upper mantle. *Earth Planet Sc Lett* 355, 244-254,  
291 doi: 10.1016/j.epsl.2012.08.025.